The Combined Influence of the Madden–Julian Oscillation and El Niño–Southern Oscillation on Australian Rainfall

TIM COWAN,[a,b] MATTHEW C. WHEELER,[b] AND ANDREW G. MARSHALL[b]

[a] *Centre for Applied Climate Sciences, University of Southern Queensland, Toowoomba, Australia*
[b] *Bureau of Meteorology, Melbourne, Australia*

(Manuscript received 15 May 2022, in final form 16 August 2022)

ABSTRACT: This study first re-examines the impact of the Madden–Julian oscillation (MJO) on weekly rainfall probabilities and wind anomalies across Australia, motivated by the need for a contemporary understanding of the MJO's influence on Australian rainfall, whether this has changed from a previous assessment published in 2009. With an extra 15 years of observations, we show that the strong impact of MJO phases 5 and 6 on northern Australia's austral summer rainfall has weakened by around 5% over Australia's Top End. In addition, austral spring has seen a weakening of the suppressed rainfall teleconnection with MJO phases 2 and 3 over southeast Australia. The weakened relationships make it a little harder to use the MJO to explain rainfall variations over northern Australia in summer and southeast Australia in spring in the current climate. The study's second motivation is to further document the combined influence of El Niño–Southern Oscillation (ENSO) and the MJO on rainfall. In summer during El Niño, as compared with La Niña or neutral ENSO conditions, there are stronger reductions in rainfall probabilities over northern Australia associated with the dry MJO phases 8, 1, and 2, but the significantly increased rainfall probabilities in MJO phases 5 and 6 remain much the same. Indeed, the MJO dominates over ENSO in its influence on weekly rainfall probabilities in the north in summer. In contrast, ENSO tends to dominate across subtropical and southern Australia in spring. The updated probability maps are an important resource for estimating the intraseasonal influence of the MJO and ENSO on Australian rainfall.

SIGNIFICANCE STATEMENT: Accompanying forecasts of multiweek rainfall, the Australian Bureau of Meteorology provide average condition maps showing the long-term relationship between the Madden–Julian oscillation (MJO) and Australian weekly rainfall. Motivated by discussions with northern Australian beef producers, we updated the maps using high-resolution data and found that in the austral summer, the association between the MJO and northern rainfall has weakened in the past 15 years. Despite this, the MJO still dominates over El Niño–Southern Oscillation (ENSO) as a driver of changes in week-to-week rainfall over northern Australia in summer, although ENSO dominates farther south in spring. This study gives users an improved understanding of what to expect in terms of upcoming weekly weather when interpreting rainfall and MJO predictions.

KEYWORDS: Madden-Julian oscillation; ENSO; Precipitation; Summer/warm season; Intraseasonal variability; Climate services

1. Introduction

The modes of intraseasonal to interannual climate variability that impact Australian rainfall are well known and documented (Risbey et al. 2009; King et al. 2014; Jaffrés et al. 2018). In a drought-prone continent like Australia (Holgate et al. 2020a), agricultural and livestock producers aim to maximize profits during wetter years and reduce their exposure to risk during drought. Although there is mixed value in multiweek to seasonal forecasts for some regional industries (Darbyshire et al. 2020; An-Vo et al. 2019; Cobon et al. 2020), up-to-date information of relevant weather and climate modes can be advantageous for primary producers trying to understand rainfall forecasts, impacting their short-term business decisions (Cobon et al. 2021).

One of the biggest influences on northern Australian pasture growth immediately before the wet season (e.g., November) is the state of El Niño–Southern Oscillation (ENSO; Brown et al. 2019). ENSO is a key factor in driving multiyear wet and dry periods and therefore influences decisions and events that lead to changes in livestock numbers across northeast Australia's grazing region (McKeon et al. 2021). On an interannual time scale, La Niña events are associated with a wetter-than-normal late austral spring to early summer over the far north and northeast regions (Cowan et al. 2020), with strong La Niña events causing earlier monsoon onsets (Lisonbee and Ribbe 2021). In general, El Niño has a weaker influence on the first major rainfall event of the wet season compared to La Niña (Cowan et al. 2022), an example of the asymmetric nature of the ENSO teleconnection on Australian rainfall (Power et al. 2006). In summer, the strength of La Niña dictates the amount of rainfall over the northern and eastern regions, but the same is not true for El Niño, where a stronger event does not

Denotes content that is immediately available upon publication as open access.

Supplemental information related to this paper is available at the Journals Online website: https://doi.org/10.1175/JCLI-D-22-0357.s1.

Corresponding author: Tim Cowan, tim.cowan@bom.gov.au

DOI: 10.1175/JCLI-D-22-0357.1

necessarily lead to drier conditions over northeastern Australia (Chung and Power 2017). Similarly, climate drivers like the Indian Ocean dipole (IOD) also affect spring rainfall across southeast Australia (Cai et al. 2011b; Risbey et al. 2009), often in conjunction with ENSO events (Lim et al. 2021a). Given that the IOD has a stronger influence on southern Australia, it is more of an important factor for commodities like wheat, allowing for potential predictability improvements and profitability (Yuan and Yamagata 2015).

The statistical relationships between modes of variability and Australian rainfall have been studied since the early 1980s. One of the most reliable predictors supporting agriculture decision-making has been the Southern Oscillation index (SOI), which has been the backbone of the SOI-based probability forecasts (Stone et al. 1996) hosted on the Queensland Government's "The Long Paddock" website (Stone et al. 2019). The Bureau of Meteorology (BoM) monitors seasonal and intraseasonal modes of variability that influence Australia's climate through an extension service added to the climate outlook pages on the BoM website. Tropical weather monitoring is a key part of this service, with the Madden–Julian oscillation (MJO) tracked each day, alongside maps of the daily outgoing longwave radiation (OLR; representing deep convection) and the average rainfall conditions for each MJO phase. Based on the research presented in this article the average rainfall condition maps were updated in May 2022, replacing maps that had been produced using rainfall data up to May 2010 (see Figs. 1–4 in the online supplemental material).

The MJO is an eastward-propagating packet of tropical convection in the Indo-Pacific domain (Madden and Julian 1994), which interacts with the Walker and Hadley circulations (Schwendike et al. 2021), and has a periodicity of between 30 and 90 days (Zhang 2005). The MJO has a strong influence on tropical and extratropical Australian rainfall through the year (Wheeler et al. 2009; Wheeler and Hendon 2004). In the austral summer months (December–February), coinciding with the monsoon, tropical northern Australia typically experiences higher chances of above normal weekly rainfall (supplemental Fig. 1), including extreme rainfall, in MJO phases 5 and 6 (Marshall et al. 2021). For southeastern Australia, there are reduced odds of wet conditions in the austral spring months (September–November) in MJO phases 2 and 3 (supplemental Fig. 4). The influence of La Niña on enhancing rainfall over eastern Australia can be counteracted when the MJO is in its suppressed phase to the north of Australia, as seen in November 2020 (Lim et al. 2021b). Interestingly, Ghelani et al. (2017) found that El Niño tends to enhance the amplitude of the MJO-induced rainfall variations in the northern tropics during the wet season (November–April), much more strongly than La Niña. Their analysis was only performed for 43 individual observing sites across northern Australia for the wet season, so the combined ENSO–MJO influence on Australia-wide rainfall across all seasons is still unknown.

In developing the Real-Time Multivariate MJO (RMM) Index (Wheeler and Hendon 2004), it was thought that industries like agriculture would benefit from a better understanding of the MJO and its influence on rainfall (Donald et al. 2006). Operational climatologists who interpret and communicate the BoM's dynamical model rainfall forecasts also benefit from knowing if and when the MJO may be promoting or inhibiting regional rainfall, and can share this knowledge with regional clients (Marshall 2021). Through climate literacy programs such as the Northern Australian Climate Program and their forecasting climate and weather workshops, northern beef and livestock producers have a greater awareness of the MJO and how it impacts their local region (Cobon et al. 2021). Throughout these workshops, a common response was the view that the average rainfall condition maps, as shown in supplemental Figs. 1–4, were outdated, only using observations through to May 2010 and with lower resolution than the latest observational datasets. Hence, the first study aim was to update the average condition maps, motivated from discussions with northern Australian beef producers who use MJO predictions and the average condition maps to help contextualize the rainfall forecasts. This work therefore builds upon Wheeler et al. (2009), who comprehensively described the MJO influence on Australian gridded rainfall in all seasons using data for June 1974–February 2006. We note, however, that the previous operational maps shown in supplemental Figs. 1–4 had extended the Wheeler et al. (2009) maps using data through to May 2010. By updating the average rainfall condition maps, we can therefore investigate whether the MJO–Australian rainfall relationships have changed with the addition of observations to the end of May 2022. The second aim is to investigate how the MJO average conditions (i.e., weekly rainfall probabilities) are affected by the state of ENSO, building on the study by Ghelani et al. (2017) by utilizing high-resolution gridded observations over Australia.

2. Data and methods

a. *Observations and reanalysis*

For this update of the older set of maps that were on the Bureau of Meteorology's Tropical Monitoring website (http://www.bom.gov.au/climate/mjo/),[1] we follow the method outlined in Wheeler et al. (2009). Our analysis is from June 1974, when satellite OLR data became available (Gruber and Krueger 1984), through to 30 April 2022. In our analysis we exclude the missing OLR period from 17 March to 31 December 1978 (Liebmann and Smith 1996); also, the May 2022 data are based on the uninterpolated OLR due to the interpolated product not being available at the time of writing.

Daily gridded rainfall are taken from the Bureau of Meteorology's Australian Gridded Climate Data (AGCD) version 1 (Australian Bureau of Meteorology 2019). Rainfall is measured across ~6500 gauge sites throughout Australia, interpolated onto a 0.05° (~5 km) grid (Jones et al. 2009), more highly resolved than the 1° (100 km) grid used in Wheeler et al. (2009).

We utilize lower- and midtropospheric winds and geopotential height reanalysis data from the National Centers for Environmental Prediction and National Center for Atmospheric Research (NCEP–NCAR; Kalnay et al. 1996). For the average

[1] The average conditions maps were replaced with updated maps in May 2022.

rainfall condition maps over Australia, composites of daily horizontal winds at 850 hPa on a 2.5° grid are displayed. We also use geopotential height and winds at 500 hPa. Daily OLR, interpolated to a 2.5° grid, is provided by polar-orbiting satellites from the National Oceanic and Atmospheric Administration (Liebmann and Smith 1996).

b. MJO index

We utilize the Wheeler and Hendon (2004) MJO RMM index, from the BoM (http://www.bom.gov.au/climate/mjo/graphics/rmm.74toRealtime.txt), computed from daily equatorially averaged (15°S–15°N) OLR and NCEP–NCAR zonal winds at 850 and 200 hPa. Specific detail is provided by Wheeler and Hendon (2004) on the procedure to define the RMM index using projections of the OLR and winds onto the first two empirical orthogonal functions of the combined anomalies. The MJO strength and phase structure are represented by the two principal component time series, RMM1 and RMM2, respectively. The daily amplitude is defined as $\sqrt{\text{RMM1}^2 + \text{RMM2}^2}$ and the phase, representing eight equally sized segments in a phase space diagram, is equal to $\tan^{-1}(\text{RMM2}/\text{RMM1})$. The latter is represented by the two-argument arctangent: *a*tan2(RMM2, RMM1), which takes into account the sign of RMM1 and RMM2. The MJO is considered to be strong when the RMM amplitude > 1, and deemed to be weak or indiscernible when the RMM amplitude ≤ 1. As shown in a MJO phase space diagram (see Fig. 2 inset), when the RMM amplitude is strong, phases 2 and 3 signify when MJO tropical convection is in the central Indian Ocean region, phases 4 and 5 in the Maritime Continent longitudes, phases 6 and 7 in the western Pacific, and phases 8 and 1 the Western Hemisphere and equatorial Africa.

c. ENSO definition

We define ENSO variability using the Troup SOI (Troup 1965), calculated using monthly station mean sea level pressure (MSLP) data from Tahiti and Darwin with the base period of June 1974–May 2022. Results are quite similar when calculating the SOI using MSLP from NCEP–NCAR for the nearest grid points to Tahiti and Darwin. The monthly SOI is smoothed using a 3-month running average following Ghelani et al. (2017), with each day assigned a corresponding monthly SOI value. Where the SOI ≤ -4, that month is designated as El Niño, and where SOI $\geq +4$, it is deemed to be La Niña, leaving neutral ENSO conditions when $-4 <$ SOI $< +4$. Our SOI threshold is less restrictive than the values of ± 8 used in Ghelani et al. (2017); however, to maximize the number of days during ENSO events per MJO phase over 47 years (i.e., to obtain three equally sized sample sets), we deemed it appropriate to use a lower SOI threshold. We have tested the sensitivity of our results using ± 8 SOI thresholds. This reduces the sample sizes for some MJO phases by 50% and also strengthens the dry and wet probabilities for both El Niño and La Niña conditions, because the weaker ENSO events are disregarded (not shown).

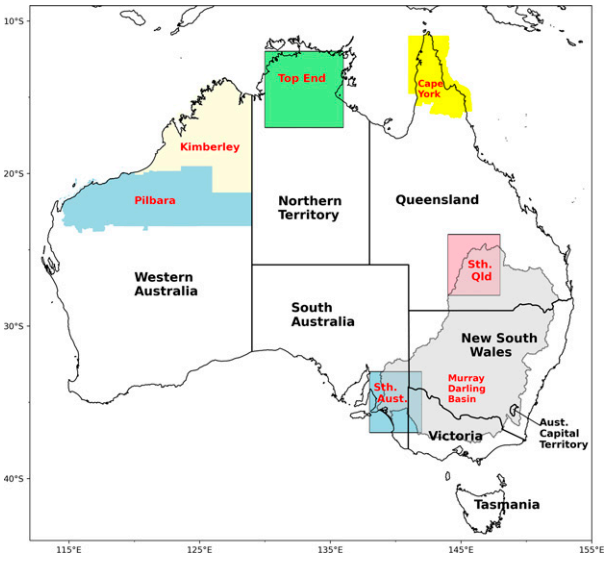

FIG. 1. Regions and locations that are referred to throughout this study. The states and territories of Australia are in black font, and shires/regions of interest are in red font.

d. Probabilities and significance

Prior to determining probabilities, we apply a 7-day running sum to determine the weekly rainfall totals, centered on the MJO day in question. For the regional average analysis (referring to Fig. 6), we also show weekly rainfall anomalies, calculated by subtracting the multiyear (June 1974–May 2022) weekly rainfall climatology from the raw totals. For circulation variables, we apply a 7-day running mean to the daily values, before subtracting the multiyear smoothed climatology from the raw daily values to create daily anomalies. For each calendar season [December–February (DJF), March–May (MAM), June–August (JJA), and September–November (SON)], we composite the rainfall, winds, OLR and geopotential height into the eight MJO phases (amplitude > 1), plus a weak MJO category (amplitude ≤ 1). With the extra years of observations, each phase now has ~200 to 400 days contributing to the composite, while the weak phase has ~1400–1800 days. Given that the start date is June 1974 and end date is May 2022, the period for DJF is 1974/75–2021/22 and for MAM, 1975–2022, whereas for JJA and SON it is 1974–2021.

The updated rainfall probability composite maps show the percentage likelihood of rainfall at a given grid point being greater or less than the median weekly rainfall. This is also framed as the number of times more likely the weekly rainfall will be above the long-term median. To avoid spuriously high probabilities in regions that receive little or no rainfall in their dry season (e.g., Western Australia's Pilbara region in winter and spring; see Fig. 1 for location), we divide the rainfall probability by the chance of being above median across all phases, including the weak phase, and then multiply through by 50% (e.g., median) to produce a more appropriate composite probability.

To determine significance, we use the same nonparametric resampling approach as detailed in Wheeler et al. (2009). This involves shifting the RMM index in time by an arbitrarily

large amount relative to the rainfall and recalculating the composite statistics in each season to determine what composite values occur by chance. An array of shifted amounts is created, starting from 50 days through to the size of the seasonal RMM time series minus 50 days, in 7-day intervals. We then compute multiple "by chance" realizations of each composite to compare against the true value. This approach maintains the autocorrelation of the RMM index and the rainfall time series (Hendon et al. 2007). We produce 500 dummy realizations from which the significance is determined at the 5% level (two-sided test, 2.5th and 97.5th percentiles). As stated in Wheeler et al. (2009), the "thresholds for significance were insensitive to varying the number of synthetic realizations between 200 and 400"; this also holds true in our study. For the El Niño and La Niña composites, we similarly compare significance using 500 dummy realizations, taken from across all ENSO states. Significance for the winds, OLR, and geopotential height composites are determined using a local t test; this includes calculating the effective sample size, taking into account the lag 1 autocorrelation of the field anomaly in the season (Wheeler et al. 2009). Circulation anomalies that are significantly different from zero at the 10% level or $t > 1.67$ are shown, with nonsignificant grid points masked out.

3. Results

a. *Weekly rainfall probabilities, 1974/75–2021/22*

We first analyze the seasonal composites of rainfall and 850 hPa wind anomalies associated with each MJO phase, with probabilities exceeding median weekly rainfall represented by shading and winds represented by vectors (Figs. 2–5). We also show each season's median weekly rainfall (bottom right panels) and composite maps of OLR anomalies and 500 hPa geopotential height and wind anomalies, which help explain the convection and midtropospheric circulation patterns (supplemental Figs. 5–12).

Starting with summer (DJF; Fig. 2), probabilities between 65% and 75% are evident across the northern Top End (12°–17°S, 130°–136°E; see Fig. 1) during phase 5, equivalent to 1.3 to 1.5 times more likely that the median weekly rainfall will be exceeded in this phase. The wet probabilities extend eastward to far northeast Queensland in phase 6, associated with broad negative OLR anomalies—signifying an active MJO pulse north of Australia—stretching into mainland southeast Asia and eastward into the western tropical Pacific (supplemental Figs. 5b,d). Anomalous cyclonic flow off northwest Australia accompanies the wet probabilities, directing strong surface westerly anomalies over the far north and anomalous easterlies over central Western Australia. A series of upper-level depressions are seen across northern Australia in phases 6 and 7, forming part of the South Pacific convergence zone as the MJO pulse moves through the western Pacific (supplemental Figs. 9d,f).

As the active MJO moves to the Maritime Continent in phases 3 and 4, rainfall probabilities of 60%–65% are apparent over inland western and central Australia associated with widespread near-surface northerly anomalies (Fig. 2). The wet probabilities do not necessarily reflect high rainfall totals as these are arid regions with less than 2 mm per week. Suppressed rainfall is restricted to the far northern Kimberley coasts, the Top End, and Cape York in phases 1 and 2 (regions shown in Fig. 1), associated with easterly anomalies, while a weakening of the climatological easterlies between 20° and 30°S maintains the typical dry conditions in central Australia. Phase 8 is also associated with widespread rainfall suppression, driven by anomalous southwesterlies, which also lead to cool temperatures in southern-central Australia (Marshall et al. 2022). The three suppression phases (8, 1, and 2) are linked to strong positive OLR anomalies moving across the Sumatra–Java region through to the western Pacific and the expansion of a midtropospheric ridge across northern Australia (supplemental Figs. 5 and 9), indicative of a monsoon break/pause and suppressed rainfall (Narsey et al. 2017).

In autumn (MAM), the rainfall probability patterns share many summer features, detailed in Wheeler et al. (2009); these include the broader enhanced rainfall likelihoods of 60%–70% in phases 4–6, stretching from the arid center (phase 4) to the northern rangelands and southeast coast (phase 5) to the northern tropics (phase 6; Fig. 3). As autumn is the wet-to-dry transition season, central Australia (e.g., 20°–30°S) is normally dry (Fig. 3; bottom right), so increased rainfall probabilities do not necessarily equate to meaningful rain. Like in summer, strong westerlies over the far north in phases 5 and 6 support the eastward movement of anomalous equatorial convection north of Australia (supplemental Figs. 6b,d,f).

The MJO phases 8, 1, and 2 in autumn are associated with rainfall likelihoods of between 30% and 40% chance of exceeding the weekly median, with central-eastern Australia experiencing probabilities of 30% in phase 8, coinciding with strong subsidence (positive OLR anomalies, divergent low-level winds) over the Maritime Continent (supplemental Fig. 6). Unlike summer, there are comparatively weak negative midtropospheric height anomalies over northern Australia, evidence of the diminishing influence of the active MJO (supplemental Fig. 10). Phase 8 is associated with a midtropospheric circulation pattern with a Southern Ocean cyclonic anomaly southwest of Australia and another east of New Zealand, with enhanced surface westerly anomalies over their northern flanks. While the circulation appears to resemble a negative Southern Annular Mode (SAM) pattern, averaging all daily SAM values for autumn in phase 8 results in a weakly positive value.[2] The circulation response to phase 8 likely relates to sea surface temperature (SST) variability north of Australia and in the southeast tropical Indian Ocean and a wave train emanating from the central Pacific (van Rensch and Cai 2014). Autumn is the transition period between the northern and southern wet seasons, when the subtropical ridge intensifies and contracts northward (Timbal and Drosdowsky 2013), with inland and eastern Australia, west of the Great Dividing Range, normally measuring <2 mm of rain per week.

[2] This is based on averaging daily SAM values over 1979–2022 using the daily NOAA SAM index (https://www.cpc.ncep.noaa.gov/products/precip/CWlink/daily_ao_index/aao/aao.shtml).

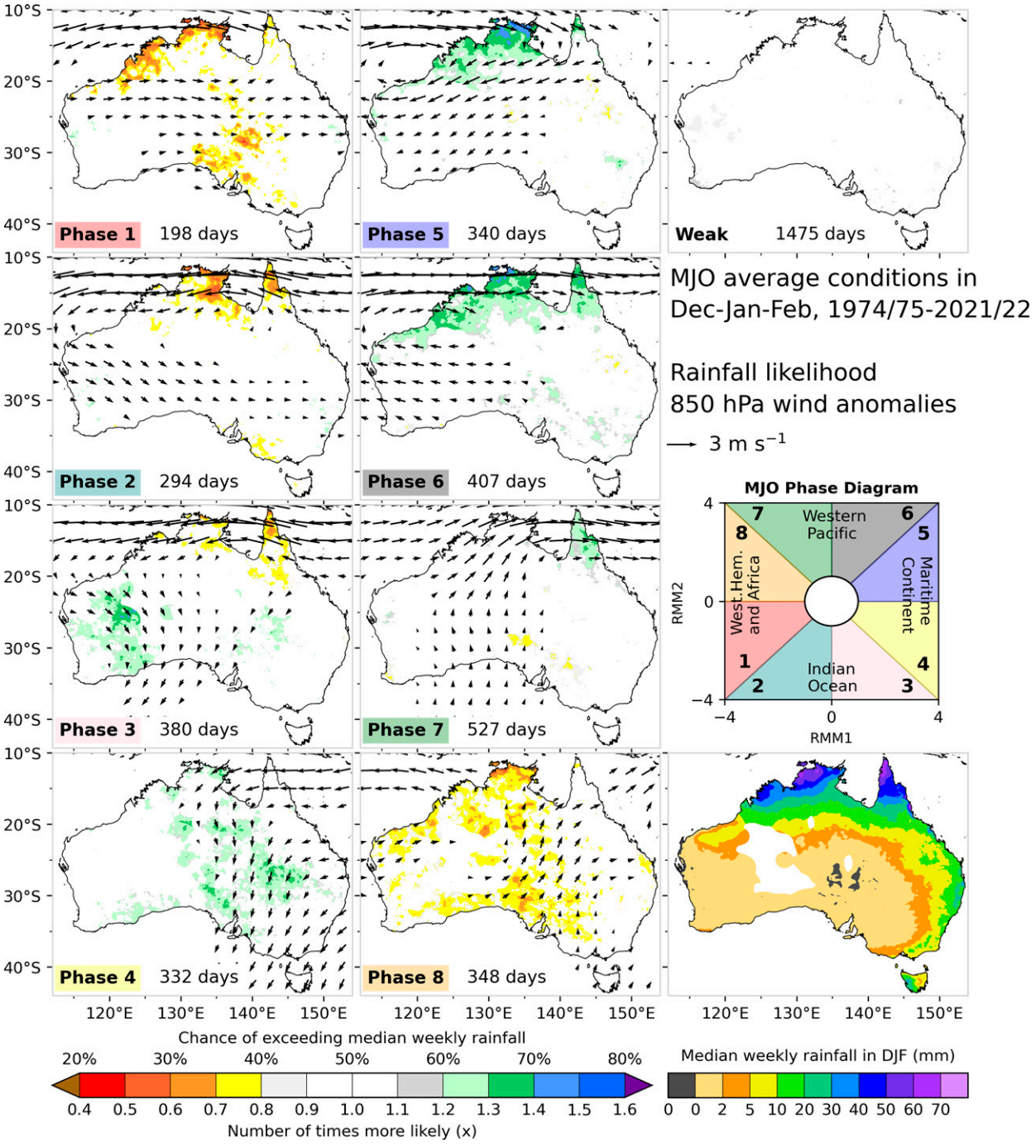

FIG. 2. (left),(center) Composites of weekly rainfall probabilities (colors) and 850 hPa wind anomalies (vectors) for phases 1–8 of the MJO for December–February (DJF) over the 1974/75–2021/22 period. (top right) Composite conditions for the weak MJO phase. For these composite maps, only statistically significant values at the 5% level are shown. Rainfall probabilities refer to the chance of weekly rainfall exceeding the median, expressed as a ratio with the mean probability (~50%, but less than 50% in climatologically dry regions). (bottom right) The median weekly rainfall in DJF, with the areas in white representing regions with insufficient rainfall observations. (middle right) The MJO phase diagram is shown as a colored diagram to aid in connecting the composite conditions with the regions of tropical convection.

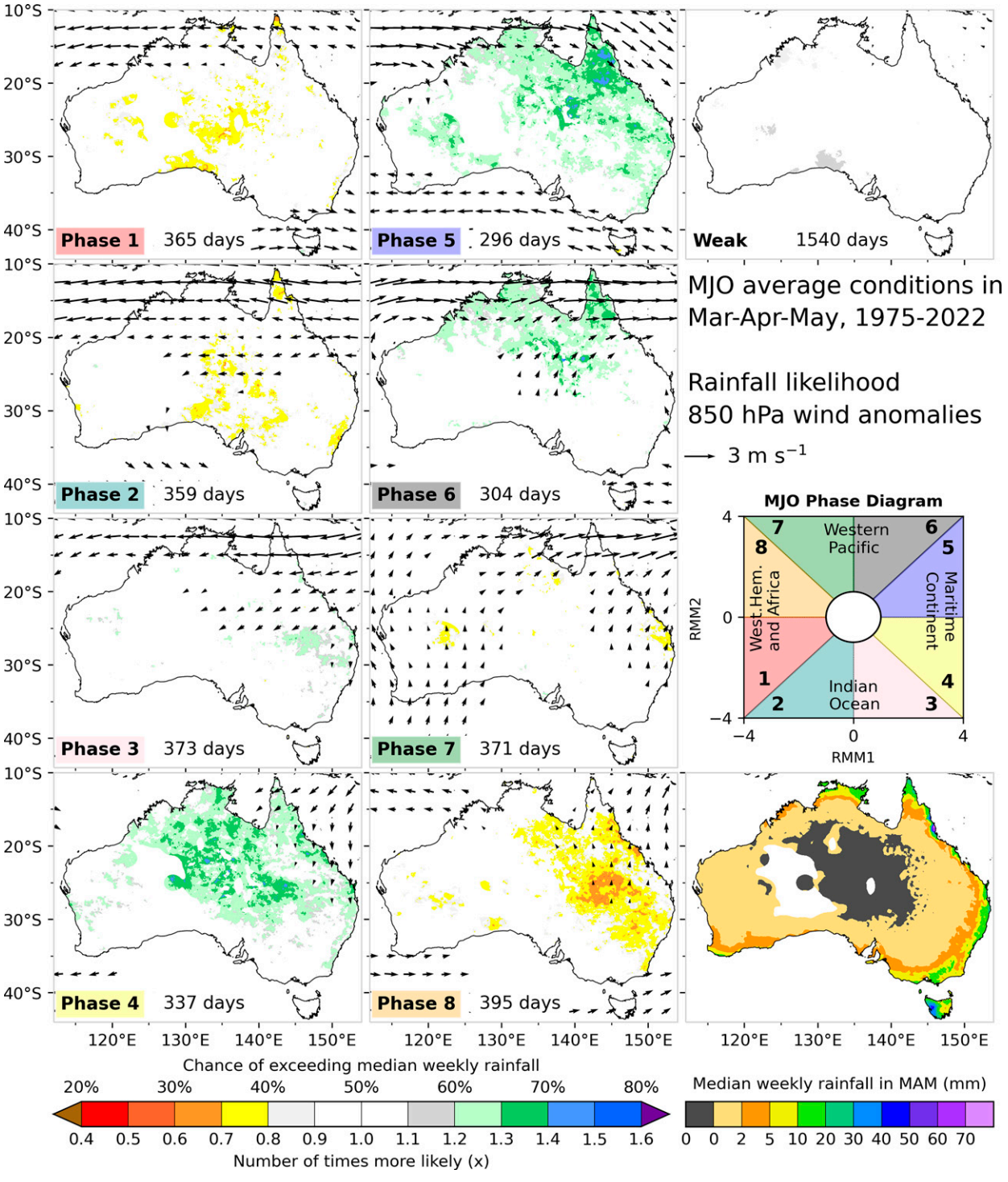

FIG. 3. As in Fig. 2, but for March–May (MAM) over the 1975–2022 period.

In winter (JJA), the MJO's influence on Australia's weather shifts from the tropics to the southern latitudes (Fig. 4), when the MJO-related convection moves to the Northern Hemisphere (supplemental Fig. 7). South of 30°S, rainfall is more likely to be suppressed through phases 8–4, peaking in phase 3. Drier conditions across Tasmania in phase 4 occur in conjunction with southeasterly anomalies. The enhanced wet conditions for the southeast are tied with phases 5 and 6,

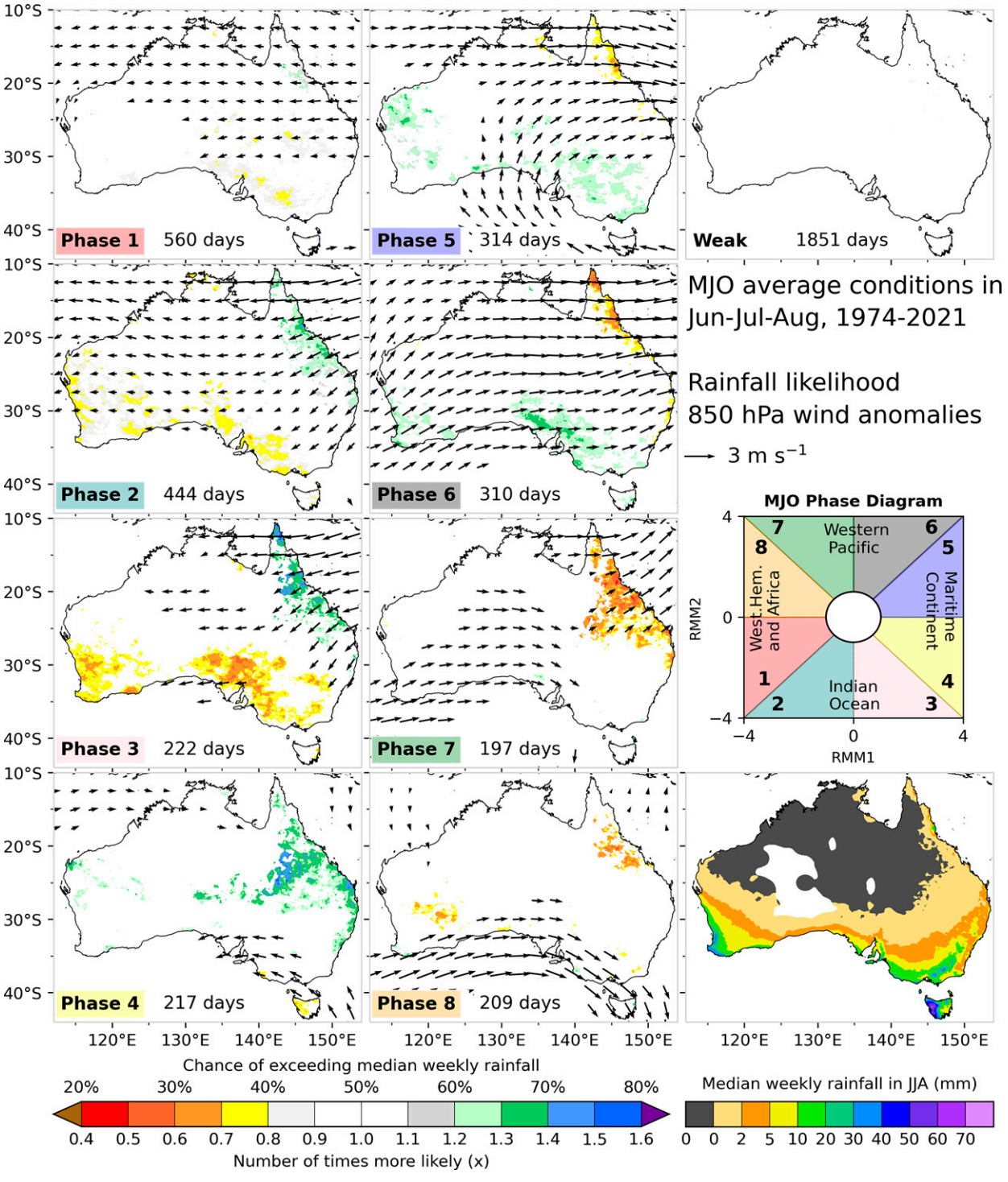

FIG. 4. As in Fig. 2, but for June–August (JJA) over the 1974–2021 period.

and a local cyclonic anomaly (supplemental Figs. 11b,d); this anomaly is consistent with both a Gill-type response to enhanced diabatic heating in the Philippine Sea (Wang and Hendon 2020) and a Rossby wave train emanating from the eastern Indian Ocean interacting with the subtropical ridge (Cai et al. 2011a). Offshore flow in phase 7 also creates a higher likelihood for drier conditions across the far northeast tropics, from Cape York down to ~25°S and

inland, although the tropics are usually dry in winter (i.e., climatological weekly rainfall < 2 mm). In phases 1–3, the northeast Queensland coast experiences onshore flow, which help to drive enhanced rainfall probabilities (60%–75%) over the region, which support anomalously warm minimum temperatures (Marshall et al. 2022).

By spring (SON), stronger enhanced rainfall signals stretch from the tropics in phases 6 and 7 to southeast Australia in phases 5 and 6 (Fig. 5). As the negative OLR anomalies accompanying the active MJO pulse pass to the north of Australia in phases 4 and 7 (supplemental Fig. 8), enhanced rainfall probabilities above 65% are observed across the Murray–Darling Basin (phases 5–6), followed by Queensland's inland Gulf region, Cape York, and the Northern Territory (phase 7). Historically, Murray–Darling Basin annual inflows are strongly correlated to spring rainfall (Cai and Cowan 2008), hence phases 5 and 6 are a key driver for this vital agricultural region. With the increased wet likelihoods in phases 4–7, anomalous westerlies traverse southern Australia (supplemental Fig. 12) as the active MJO packet reaches the western Pacific (supplemental Fig. 8). Like summer, the suppressed rainfall probabilities are predominantly in phases 8, 1, and 2, and are associated with an anticyclonic anomaly across southern Australia that tracks eastward as the MJO transitions from phases 2 to 3 (supplemental Fig. 12), promoting strengthened easterlies across the far north.

b. *Regional breakdown*

We next analyze rainfall metrics for each MJO phase in three important agricultural and primary production regions introduced in Wheeler et al. (2009). The regions include the Top End (12°–17°S, 130°–136°E; cattle, crops), southern Australia (33°–37°S, 138°–142°E; wheat, wine, sheep), and southern-central Queensland (24°–28°S, 144°–148°E; wheat, sheep, cattle). These regions are displayed in Fig. 1. The rainfall metrics include the above median rainfall probability, the probability of daily rainfall above 1 mm, the probability of weekly rainfall in the highest decile (top 10% wettest), and the mean daily rainfall anomaly (Fig. 6). We compare the latter three metrics (i.e., all except for above median) to Fig. 7 in Wheeler et al. (2009). For MJO phases 5 and 6 in summer, all rainfall metrics are statistically significant in the Top End (Fig. 6; top left). Although the daily anomalies in phases 5 and 6 match those in Wheeler et al.'s (2009) Fig. 7,[3] the highest decile probabilities are slightly weaker, and the probabilities of above 1 mm are about 10% weaker at around 65%–67%. Another noticeable difference from their Fig. 7 is seen for the Top End highest decile rain probabilities (Fig. 6, green line) in autumn, with significant peaks in phases 5 and 6, with probabilities of 17%, compared to 15%–16% in Wheeler et al.'s Fig. 7. As a comparison, the Top End's climatological mean daily rainfall in autumn is 2.8 mm compared to the 1974–2006 estimate of 3.1 mm in Fig. 7 in Wheeler et al. (2009). The Top End's summer climatological mean daily rainfall remains unchanged at 7.5 mm.

Southern Australia experiences a significant (at the 5% level) summer reduction in daily rainfall anomalies in phase 8 and positive anomalies in phase 4 (Fig. 6; top center). The negative rainfall anomalies in phase 8 are associated with southerly winds and significantly cool temperature anomalies (Marshall et al. 2022), suggesting that the positive OLR anomalies north of Australia (supplemental Fig. 5) have a strong extratropical teleconnection. Given the summer climatological mean daily rainfall is low (0.7 mm), the significant positive anomalies in phase 4 are likely to result from one or two wet years, as noted by Wheeler et al. (2009). In southern Australia's winter rainfall season, a significant above median probability of 60% is evident in phase 6, helped by eastward-bearing weather systems and strong anomalous westerlies (Fig. 4). However, a significant response in phase 6 is not seen in the daily anomalies or chance of extreme rainfall. For a livestock or crop producer, what is perhaps more important are the significant dry probabilities between phases 1 and 3. The feature driving the southern Australia's winter suppression is the anticyclonic upper-level ridge, which weakens the westerly rain-bearing weather systems (supplemental Figs. 11a,c,e). The rainfall metrics in spring follow the general behavior in winter broadly across all the MJO phases, in that there are slightly higher probabilities in phases 5–7; the one difference is that none of the rainfall probability metrics over southern Australia are significant in spring. To the east of the southern Australia region, the suppressed spring rainfall signals (phases 2 and 3) are associated with a midtropospheric high centered over southeast Australia, directing easterly anomalies to the Murray–Darling Basin. The enhanced rainfall phases (phases 5 and 6) over the Murray–Darling Basin are fed by enhanced westerly flow (Fig. 5), tied to the midtropospheric low over the southeast (supplemental Figs. 12b,d).

The third region, southern Queensland, has experienced little change in the rainfall metrics from the Wheeler et al. (2009) study. The most noteworthy features appear in autumn, where there are significant (5% level) above median probabilities exceeding 60% in phases 3 to 5, and significant dry probabilities and anomalies (1% level) in phase 8 (Fig. 6; second from top, right). Analyzing overlapping seasonal composites, the wetter-than-normal likelihoods in phases 4 and 5 stem from enhanced local convection close to southern Queensland in later autumn (May) more so than late summer (February and March; not shown). Even though southern Queensland's climatological mean daily rainfall in autumn is only 1.2 mm, a significant reduction of 0.5 mm occurs in MJO phase 8. The chance of daily rainfall exceeding 1 mm is less than 10%, while the chance of extreme rainfall (i.e., highest decile) is around 5%. Southern Queensland lies between an upper-level ridge over western Australia and a cyclonic anomaly to the east of New Zealand (supplemental Fig. 10h), allowing for calmer, more stable conditions along Australia's eastern seaboard.

[3] The Wheeler et al. (2009) study used data up to February 2006.

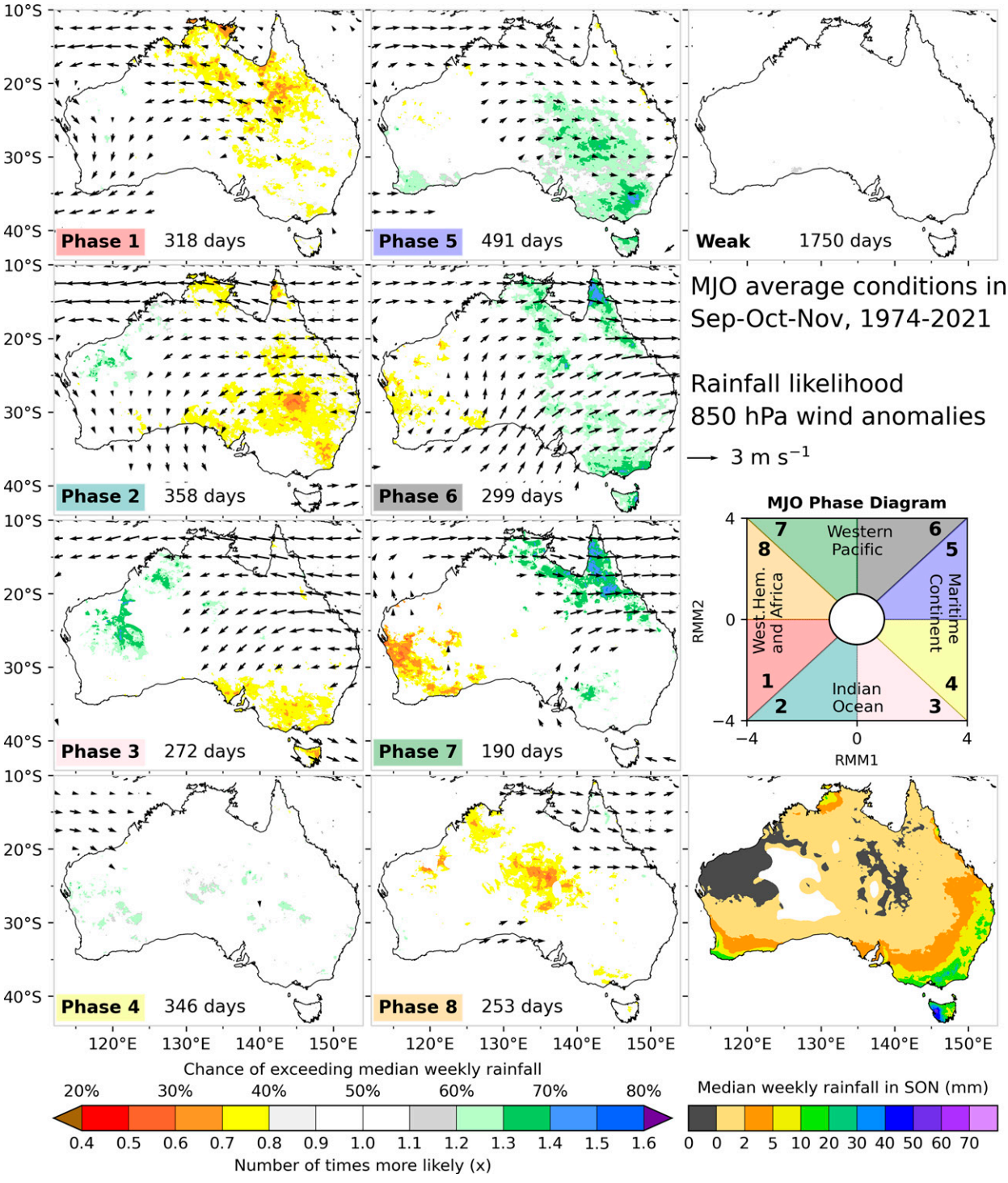

FIG. 5. As in Fig. 2, but for September–November (SON) over the 1974–2021 period.

c. Changes in average conditions between 2009 and 2021/22

The BoM's previous average conditions maps (replaced at the end of May 2022) utilized data through to May 2010. With over a decade of additional rainfall observations, we can now assess how the MJO's influence on rainfall has changed. We focus on summer and spring,[4] identifying regions with the

[4] For 1974–2009 (2021/22), summer is December 1974–February 2010 (February 2022), and spring is September 1974–November 2009 (2021).

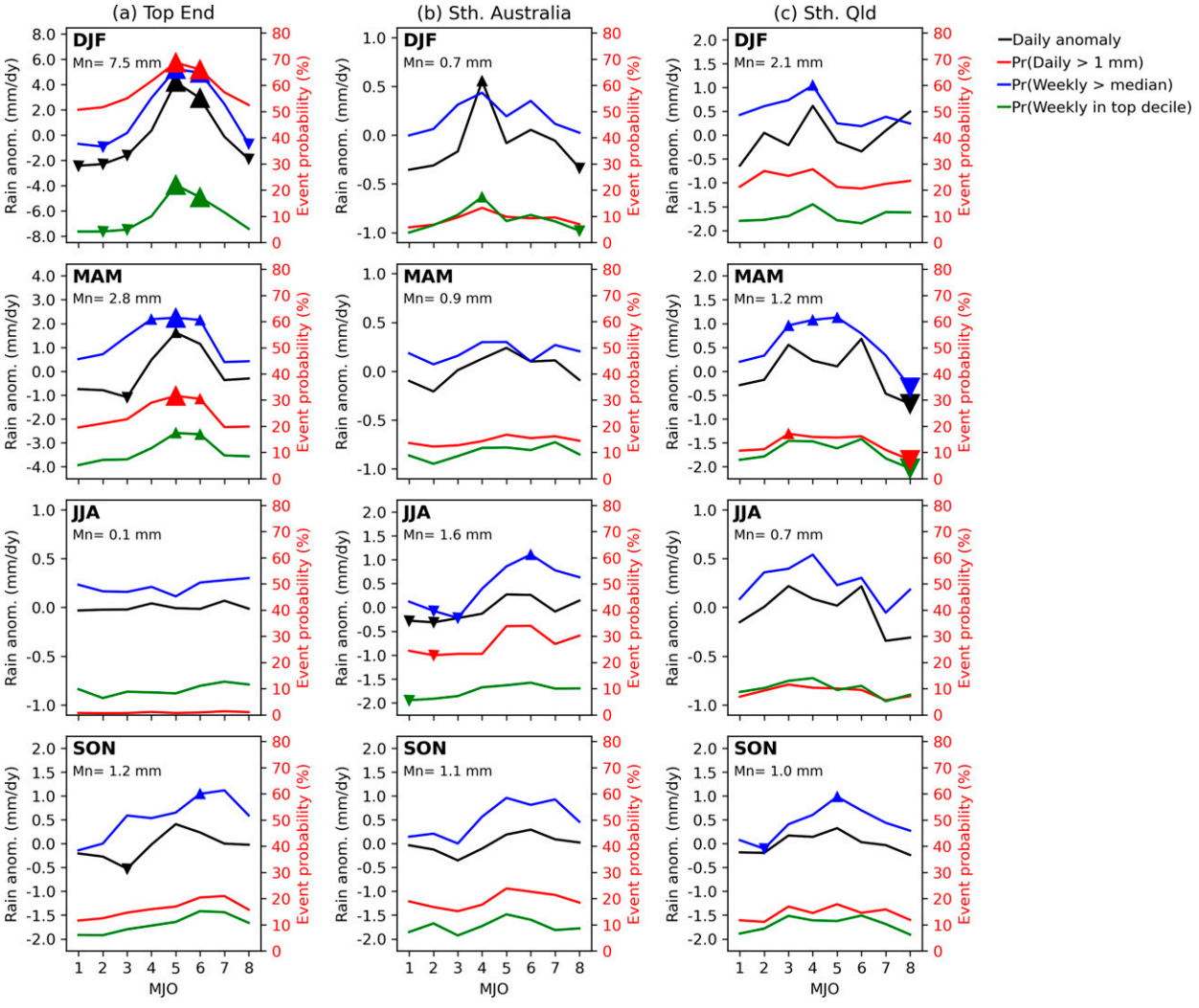

FIG. 6. Seasonal rainfall metrics as a function of MJO phase, spatially averaged over three regions (land only): (a) Top End (12°–17°S, 130°–136°E), (b) southern Australia (33°–37°S, 138°–142°E), and (c) southern Queensland (24°–28°S, 144°–148°E). The regions are shown in Fig. 1. (top) Area-averaged daily rainfall anomaly (black line), area-averaged probabilities of daily rainfall > 1 mm day^{-1} (red line), above median weekly rainfall (blue line), and weekly rainfall in the highest decile (green line) for DJF. (second to bottom rows) As in the top row, but for MAM, JJA, and SON, respectively. Large and small triangles indicate signals that are significant at the 1% and 5% level, respectively, for at least half of the grid squares in each area. For the black curve, the relevant scale is on the left vertical axis of each panel (black), and for the colored curves, on the right vertical axis (red). The climatological mean daily rainfall ("Mn") in each region is printed in the upper left of each panel. All metrics, except for probability of weekly rainfall above median (blue line), can be compared to Fig. 7 of Wheeler et al. (2009).

greatest change in rainfall between 1974/75–2021/22 and 1974/75–2009/10 as well as changes in the large-scale circulation (e.g., 500 hPa geopotential heights and winds). As there have been little change in autumn and winter average condition (less than 5% between the two periods), they are not shown. We assess the difference using the 0.05° gridded data (i.e., not the 1° used for the 1974–2009 operational average condition maps shown in supplemental Figs. 1–4).

For summer, there is a 65%–75% probability of enhanced rainfall during phases 5 and 6 over Australia's far north based on 1974/75–2021/22 data (Fig. 2). The 1974/75–2009/10 maps suggest the probability to be above 80% (supplemental Fig. 1). This reflects a probability reduction of more than 8% over the northwest in phase 5 (Fig. 7). Easterly anomalies are evident across the Top End and Cape York, associated with a weakening and contraction of the monsoon low, as represented by positive 500 hPa geopotential height differences off northwest Australia in phase 5 (Fig. 7). In phase 6, the probability reduction is weaker than in phase 5, at around 5% and mostly confined to the Top End and southern Cape York (Fig. 7). There has also been a contraction of the northwest Australian low pressure anomaly (Fig. 7); however, a slight westward extension of the anomalous low off the northeast coast (see supplemental Fig. 9d) has contributed to ~5% increase in rainfall probabilities in

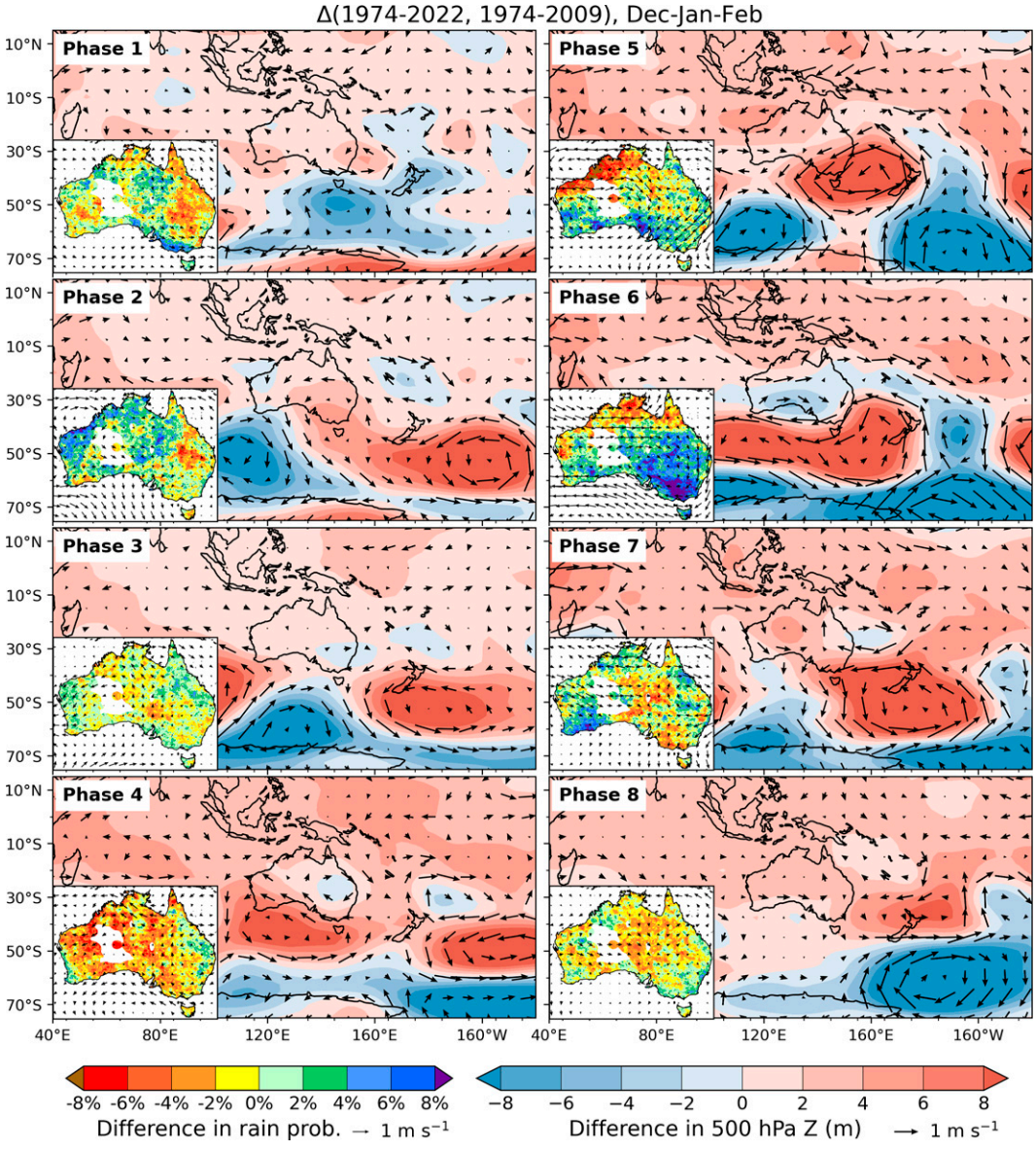

FIG. 7. Difference between average conditions in 1974/75–2021/22 and 1974/75–2009/10 showing (small inset panels) above weekly rainfall probabilities and 850 hPa wind anomalies and (larger panels) geopotential height and wind anomalies at 500 hPa. Shown are all MJO phases for DJF. Blue colored rainfall probabilities reflect higher probabilities in the longer period, and red colored rainfall probabilities reflect higher probabilities in the shorter period. Red colored 500 hPa geopotential height anomalies reflect higher heights in the longer period, and blue-colored 500 hPa geopotential height anomalies reflect lower heights in the shorter period.

central Queensland. Whether this is permanent or merely decadal variability (e.g., Cai et al. 2010) is yet to be determined. However, the circulation differences between 1974/75–2009/10 and 1974/75–2021/22 do not explain causation, merely that the fact that the rainfall declines are consistent with how the midtropospheric heights have changed in the past decade. In the remaining MJO phases, the rainfall and circulation changes across the far tropical north of Australia are weak and likely due to noise.

For spring, specifically the rainfall suppression phases 2 and 3, there are probabilities of between 30% and 40% (orange–yellow shades in Fig. 5) stretching from central eastern Australia (phase 2) to southern-eastern Australia (phase 3). This represents an increase of 4%–6% over these regions in phase 2 and exceeding 8% in phase 3 (Fig. 8) when compared to 1974–2009 conditions (supplemental Fig. 4). This implies that these southern regions are more likely to receive median rainfall during the MJO suppression phases, despite the fact that spring rainfall over southern Victoria has been in decline since the mid-1980s (Dey et al. 2019). The circulation difference between 1974–2021 and 1974–2009 suggests that the increase in

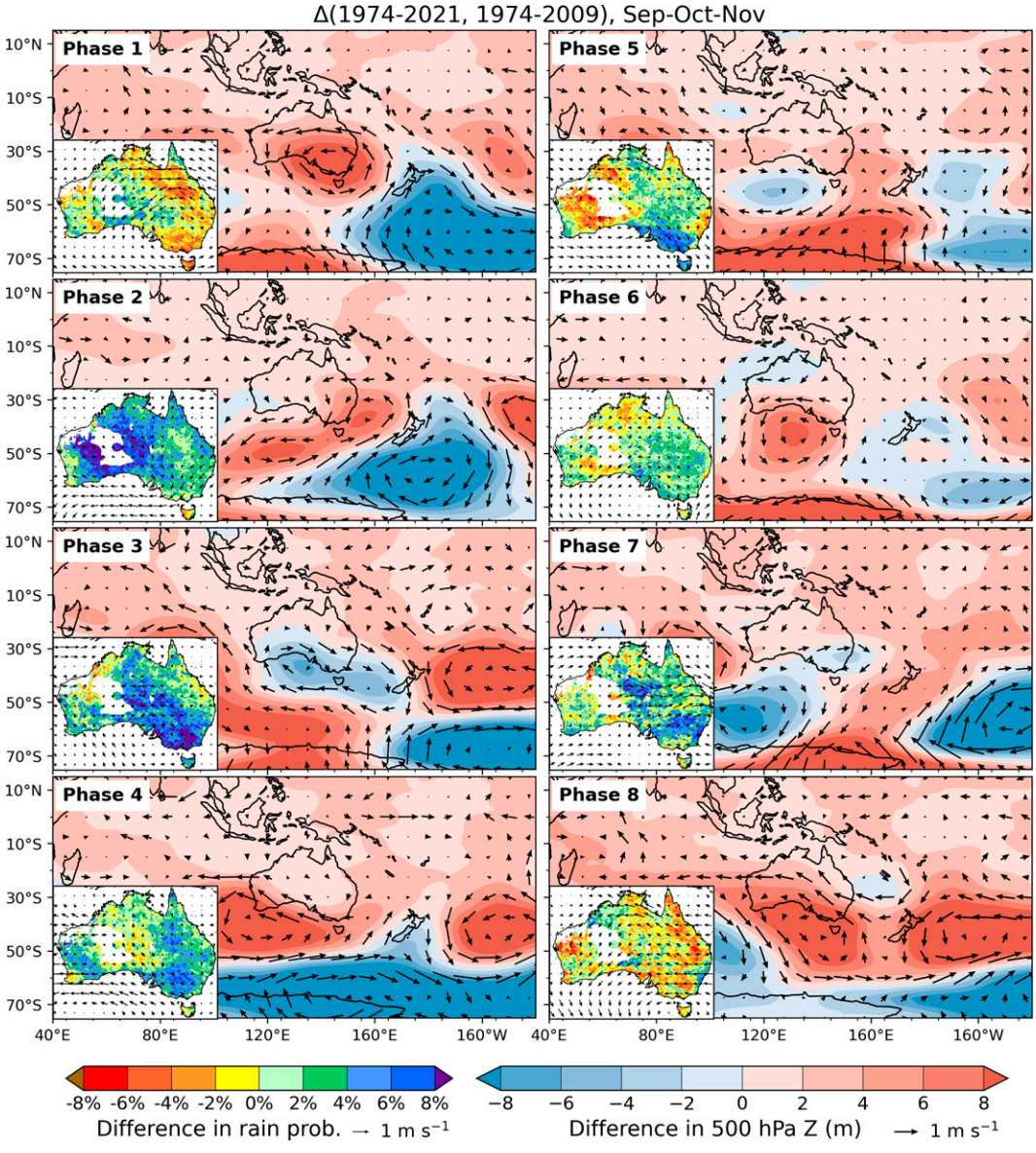

FIG. 8. As in Fig. 7, but for SON.

southeast Australian rainfall probabilities results from a strengthening and eastward expansion of an anticyclonic anomaly into the Tasman Sea in phase 2, whereas in phase 3 the anticyclone weakens and contracts eastward on its western flank (Fig. 8). The phase 3 changes in the midtropospheric circulation resembles a cut-off low anomaly centered near the Great Australian Bight (Griffiths et al. 1998), directing cyclonic anomalies to Victoria. This implies that the teleconnection of the MJO in phase 3 to Victoria and Tasmania has weakened since 2009. For the remaining phases, we see a slightly greater chance of wetter conditions over Queensland in phase 5 in the 1974–2021 period, whereas in phase 1 there is a decline of around 5% in central-western Queensland. For the spring season, central-western Queensland is particularly dry (<2 mm per week), so while these changes perhaps appear dramatic, they reflect small absolute changes.

There is a possibility that different climatologies (shorter 36-yr vs longer 47-yr period) might partially explain the changing probabilities; however, recalculating the 1974/75–2021/22 composites using a 1974/75–2009/10 climatology does not affect the result (not shown). Given that both periods contain overlapping observations, we also performed the same analysis using non-overlapping periods, 1974–99 and 2000–21, and found the changes in summer and spring to be of a similar magnitude as shown here. Another possibility is that the 1° grid resolution 1974/75–2009/10 composite maps possibly overestimated the probabilities (e.g., phases 5 and 6 in summer, phases 2 and 3 in spring). To confirm that this does not explain the differences found in this present study, the 1974/75–2009/10 maps were reconstructed using 5-km data (not shown) and were found to be in strong

agreement with the BoM's 1° composites (supplemental Figs. 1–4).

Last, we looked at changes in the MJO amplitude and frequency (i.e., time spent in each phase) between the two periods to see if this might explain the changes in the rainfall probabilities. For 1974/75–2021/22 DJF, the MJO typically spends 8% and 9.6% of the time in phases 5 and 6, respectively; this is a jump from 7% to 8.3%, respectively, from the 1974/75–2009/10 period. Similarly, the average MJO amplitude in DJF for phases 5 and 6 has increased by 2.6% and 5.5%, respectively. Hence, despite the MJO residence time and intensity increasing in the enhanced phases 5 and 6 (conducive to Top End rainfall), the rainfall probability has reduced. Future work needs to elucidate why northern Australian DJF rainfall probabilities have declined in the recent decade, given the recent increasing trends in rainfall since the mid-1980s (Dey et al. 2019; Heidemann et al. 2022).

d. *Rainfall response to combined ENSO states/MJO phases*

The probabilities of above median weekly rainfall for each MJO phase in summer, separated into El Niño, La Niña, and neutral conditions, are shown in Figs. 9–11, respectively. Although the focus is on summer, probability maps for other seasons for different ENSO states are shown in supplemental Figs. 13–21 (supporting the regional analysis in Fig. 12); however, we caution against the interpretation of probabilities in regions of very low median rainfall. During an El Niño summer, there are significantly low rainfall probabilities (<30%) in phases 8, 1, and 2, along Australia's far north coast, from the Pilbara in the west to Cape York in the east, and south of 20°S (Fig. 9). A greater suppressed rainfall likelihood is also evident across the southeast in phases 8 and 1, however climatological rainfall in summer is less than 5 mm week^{-1}. Suppressed rainfall is accompanied by significant 850 hPa easterly anomalies, signifying a monsoon pause. Averaged over the Top End, the suppressed rainfall probabilities are statistically significant at the 1% level (phases 8, 1, and 2) (Fig. 12a) and signify the compounding effect of the MJO–El Niño teleconnection to monsoon rainfall. Based on historical observations, strong El Niño events (SOI < -13) are associated with positive summer rainfall anomalies in the Top End (Chung and Power 2017). This is observed; as the MJO moves from phase 3 to phase 7, the chances of exceeding median weekly rainfall over northern Australia increases to 65%, with significant probabilities in the Top End in phases 5 and 6 (Figs. 9 and 12a). While there is an increased chance of enhanced rainfall for southern Australia in phases 2 to 5, and over southern Queensland in phases 2–4 (Figs. 12b,c), climatological summer rainfall outside of the tropics is quite low with daily rainfall anomalies of ~0.5 mm. It is also worth noting that the positive rainfall anomalies in southeast Australia are consistent with stronger central Pacific El Niño events that have been shown to break droughts (Freund et al. 2021), with a greater frequency of events since the late 1990s (Freund et al. 2019).

For summer La Niña conditions, enhanced rainfall probabilities are seen in nearly all MJO phases (Fig. 10), with high chances above 85% in western-central Western Australia in phases 1 to 3, likely because the region is typically dry in summer (0–5 mm per week). As with El Niño, enhanced rainfall likelihoods are seen over northern Australia in phases 5 to 7; however, apart from phases 5 and 6, most of the probabilities are regionally inhomogeneous. This is best highlighted in the Top End, where we see near-identical chances of wet conditions (~65%) for both La Niña and El Niño conditions (Fig. 12a). This supports the idea that the MJO is the dominant driver of heavy summer rainfall periods in the Top End. ENSO dominates the rainfall signal only when the MJO is weak, particularly over the far northwest regions, with El Niño suppressing rainfall and La Niña enhancing rainfall.

For neutral ENSO conditions in summer, phases 5 and 6 are associated with wet probabilities above 60% across the far north, including the Top End and northwest (Fig. 11). The phase 5 average conditions are associated with cyclonic anomalies, with enhanced monsoon westerlies over the Top End and anomalous easterlies over the inland subtropics. The rainfall probabilities are statistically significant in the Top End (Fig. 12a), again confirming the importance of the MJO over ENSO as a dominant intraseasonal driver of rainfall variations in summer. Easterly anomalies in phase 5 lead to higher chances of suppressed rainfall over southern Queensland (Fig. 12c), also seen in MJO phase 6; these patterns are consistent with the average conditions in summer irrespective of ENSO state (Wheeler et al. 2009), but are quite different from the wet conditions observed for the same MJO phases in La Niña years. In southern Australia, the relationship between rainfall and MJO appears mostly unaffected by neutral ENSO conditions in summer, as there are only marginal differences between the probabilities, with most phases within 10% of the median (Fig. 12b).

Focusing on the three agricultural regions for the remaining seasons, beginning in autumn, during a La Niña event, the Top End experiences significant enhanced rainfall probabilities from phases 3 to 7 (Fig. 12a, second row), similar to southern Queensland (Fig. 12c, second row). In the Top End, an El Niño in autumn leads to the similar pattern to summer with enhanced rainfall probabilities restricted to phases 4 to 6, while for southern Queensland, El Niño counteracts the MJO influence. In autumn, neutral conditions match the conditions seen for El Niño through the MJO phases in the Top End, whereas neutral and La Niña conditions are more alike across the MJO phases for southern Queensland. Southern Australia is the exception, where all MJO phases occurring in neutral ENSO conditions result in suppressed rainfall (Fig. 12b, second row), with statistically significant probabilities in phases 2 and 6. Even though southern Australia normally receives less than 5 mm week^{-1}, the first meaningful rainfall in autumn (i.e., autumn break) is critically important for sowing wheat in this region (Pook et al. 2009). This analysis indicates that neither El Niño nor La Niña is more or less dominant in any MJO phase with respect to autumn rainfall probabilities over southern Australia.

Last, for winter and spring there is a strong emergence of ENSO's influence on rainfall probabilities over southern

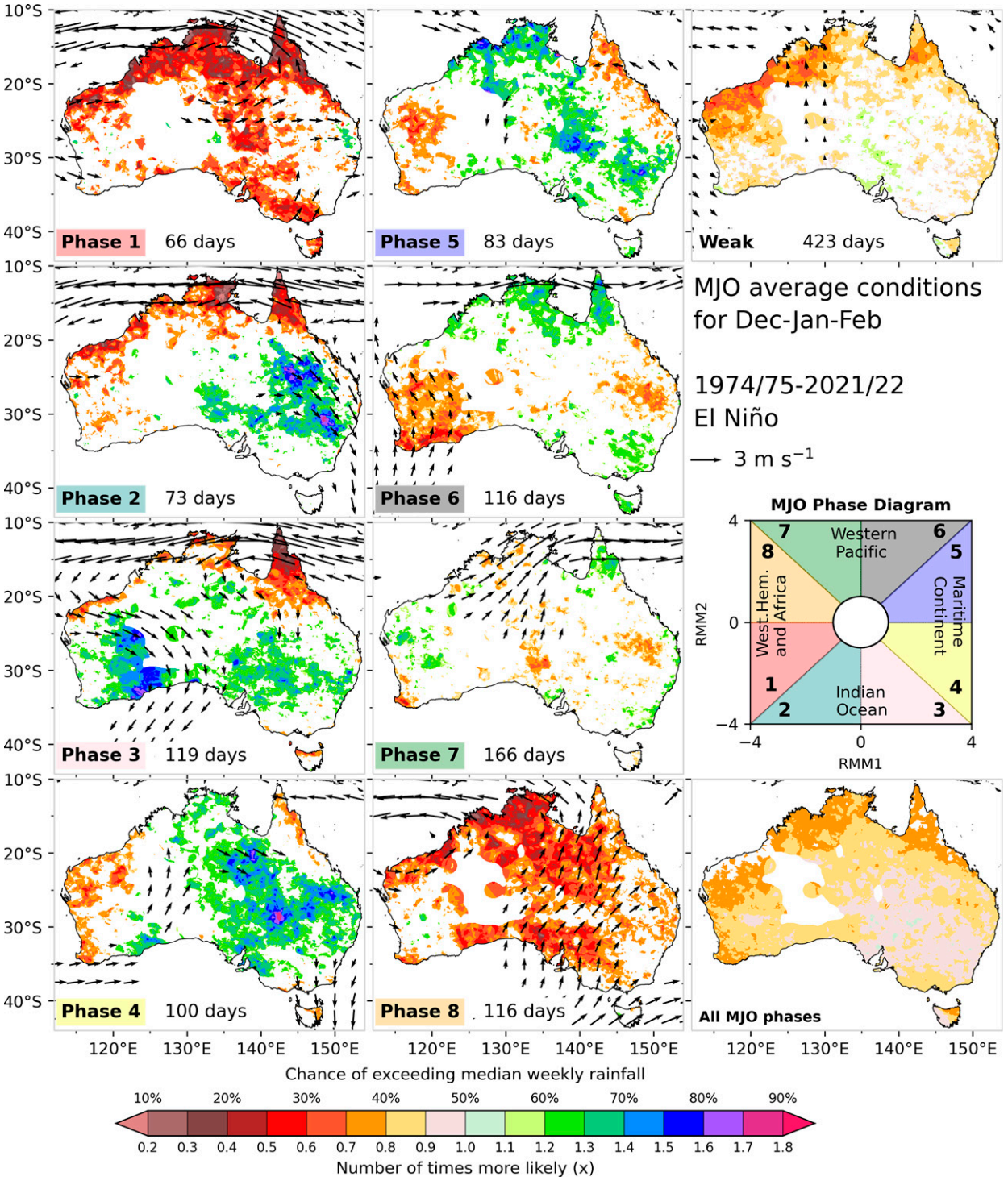

FIG. 9. (left),(center) Composites of weekly rainfall probabilities (colors) and 850 hPa wind anomalies (vectors) for phases 1–8 of the MJO for December–February (DJF) over the 1974/75–2021/22 period for El Niño conditions. (top right) Composite conditions for the weak MJO phase. For these composite maps, only statistically significant values at the 10% level are shown due to the smaller samples. (bottom right) The probability of exceeding normal weekly rainfall in DJF across all MJO phases for El Niño conditions, with areas in white representing regions with insufficient rainfall observations. El Niño years are defined as when the 3-month running-mean SOI is equal or less than −4. (middle right) The MJO phase diagram is shown as a colored diagram to aid in connecting the composite conditions with the regions of tropical convection.

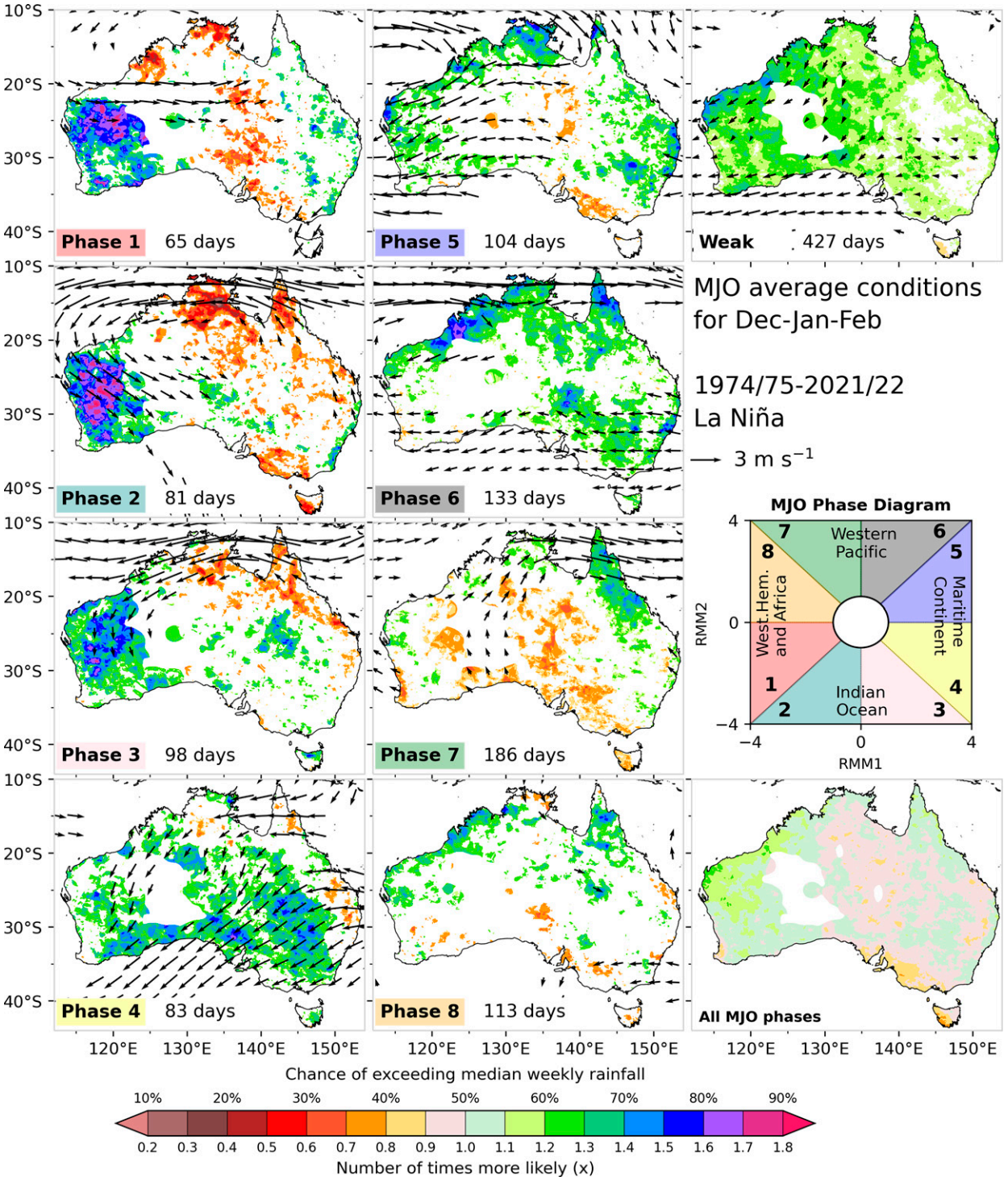

FIG. 10. As in Fig. 9, but for La Niña conditions, defined as when the 3-month running-mean SOI is equal or greater than 4.

Australia and southern Queensland, with La Niña acting to enhance rainfall and El Niño suppressing rainfall across most MJO phases (Figs. 12b,c, bottom rows). Significantly low probabilities (<35%) during phases 5 to 7 in southern Queensland in winter highlight the clear distinction between El Niño and La Niña and their impact on rainfall. In spring, the season with the strongest association between ENSO and Australian rainfall (Risbey et al. 2009), we see the greatest impact on rainfall probabilities by El Niño compared to La Niña, particularly in phases 6–8, and phase 1 for southern

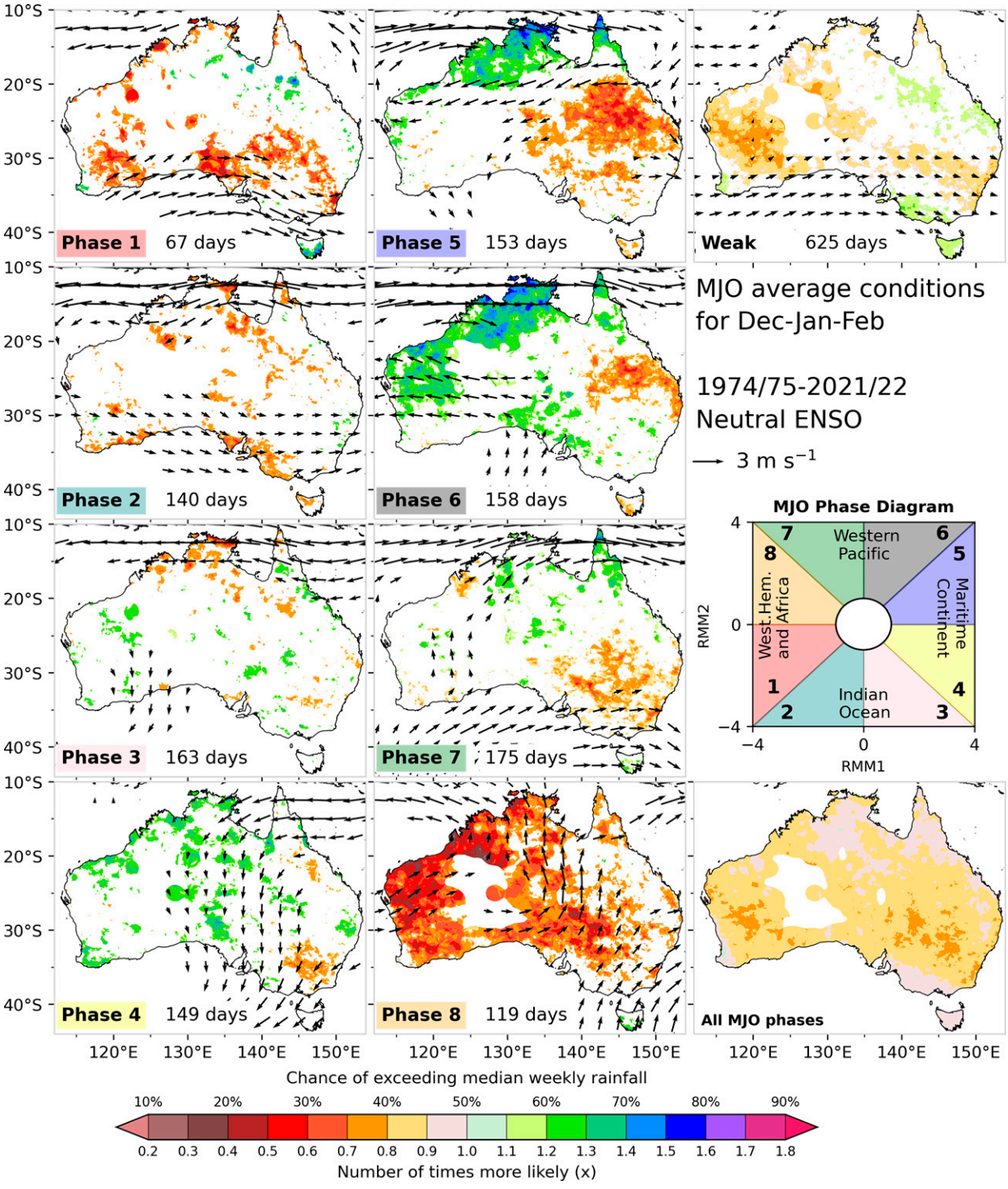

FIG. 11. As in Fig. 9, but for neutral ENSO conditions, which are defined as when the 3-month running-mean SOI is between (but not equal to) −4 and 4.

Queensland (significant probabilities < 30%) and phases 1–3 for southern Australia (significant probabilities < 40%). In contrast, the probabilities for the aforementioned regions for La Niña do not exceed 66%. Even in the Top End, spanning MJO phases 4–8, there is a clear separation of the rainfall probabilities in spring, indicating the stronger influence of ENSO compared to the MJO (Fig. 12a, bottom row).

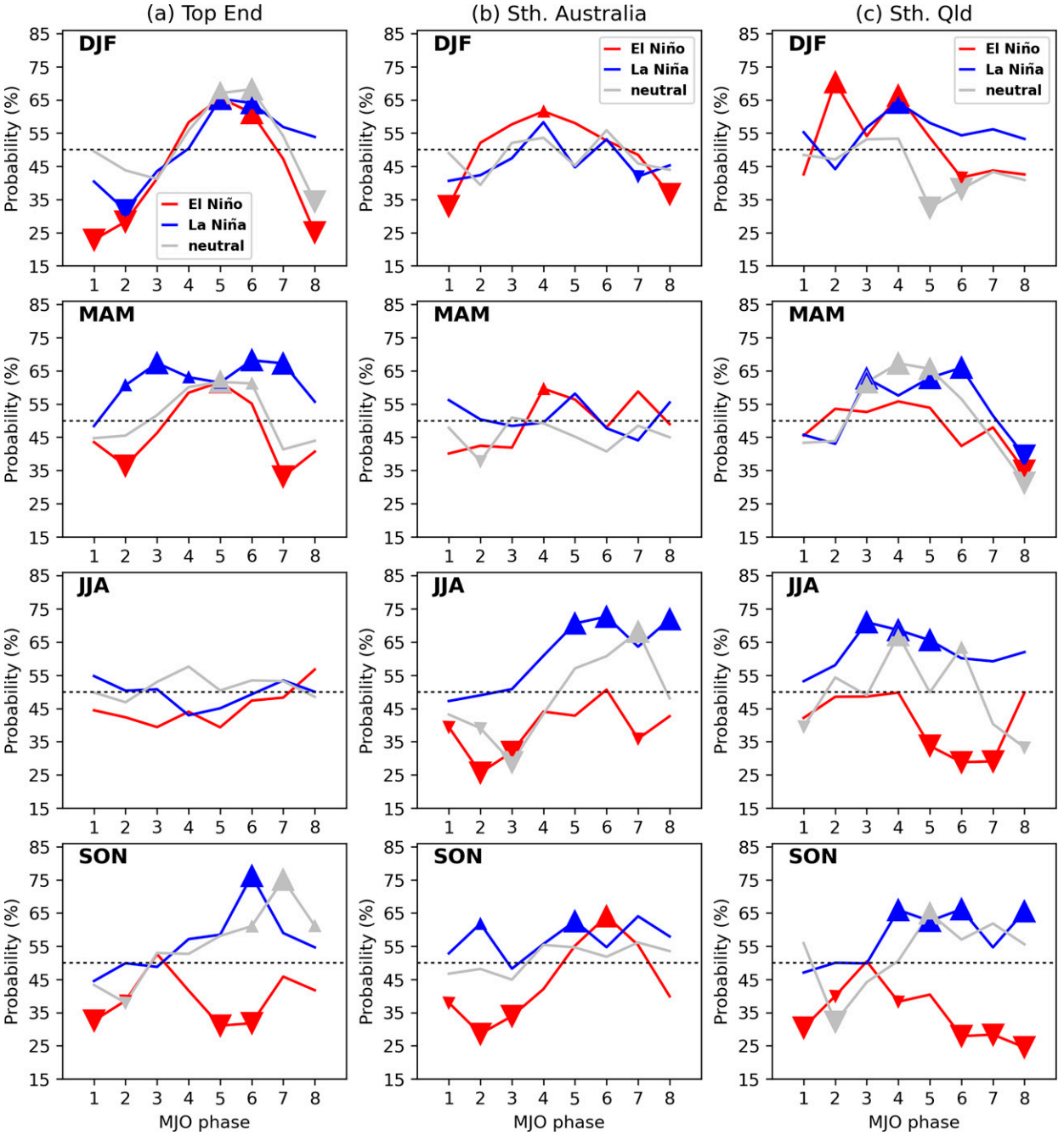

FIG. 12. Area-averaged probability of above median weekly rainfall (for each season) as a function of MJO phase and separated by ENSO phase, spatially averaged over three regions: (a) Top End, (b) southern Australia, and (c) southern Queensland. (top) Area-averaged probabilities of daily rainfall above median weekly rainfall for El Niño events (red line), La Niña events (blue line), and neutral conditions (gray line) for DJF. (second to bottom rows) As in the top row, but for MAM, JJA, and SON, respectively. Large (small) triangles indicate signals that are significant at the 1% (5%) level for at least half of the grid squares in each area. The 50% probability is shown by the horizontal dotted line. The definition of an ENSO event is described in the main text.

4. Discussion

Aside from specific events (Lim et al. 2021b) and a northern Australian assessment using weather station data (Ghelani et al. 2017), little was previously known about the concurrent impact of ENSO and MJO on Australia-wide rainfall. Presently, a similar analysis on Australian maximum and minimum temperatures has been undertaken (Marshall et al. 2022). Studies, like that of Hendon et al. (2007), have focused on the role that the MJO plays in promoting El Niño development or have provided insights into the broader Indo-Pacific teleconnection

patterns (Moon et al. 2011). Here we have quantified the combined MJO and ENSO influence on Australian rainfall and shown this to be seasonally dependent (i.e., comparing spring and summer; Fig. 12) but have not focused on whether ENSO itself can affect the MJO.

One result we have obtained, consistent with Ghelani et al. (2017), is that the MJO has a greater overall impact on summer rainfall in northern Australia during El Niño than La Niña. What might explain this? One possibility is that ENSO influences the amount of time the MJO spends in each phase or the average phase magnitude, which could explain the change in rainfall magnitude response. For phases 5 and 6 in summer, where we see similar observed rainfall probabilities across the Top End (Fig. 12a), 26% of days occur during an El Niño, 32% during La Niña, and 42% during neutral conditions (see day counts in Figs. 9–11). The respective average MJO amplitudes are 1.75 (El Niño), 1.61 (La Niña), and 1.84 (neutral). While higher MJO amplitudes during neutral ENSO conditions might partially explain the phase 6 higher rainfall probabilities over the Top End, the near-identical probabilities in phase 5 appear to be unaffected by the amplitude strength difference between El Niño and La Niña, or by the number of days spent in that enhanced rainfall phase (i.e., more days during La Niña). For the rainfall suppression phases 8, 1, and 2 in summer, it is apparent that an El Niño is directly associated with drier conditions over northern Australia. Yet the average amplitude over these three MJO phases during El Niño is 1.62, compared to 1.65 for La Niña and 1.70 for neutral conditions. This implies that for the northern Australian summer, the probability of above normal rainfall cannot be explained by the MJO strength under the influence of ENSO, consistent with Ghelani et al. (2017). Likewise, the number of days in phases 8, 1, and 2 during El Niño and La Niña is nearly identical (255 vs 259, respectively) and hence MJO frequency cannot explain the differences in dry conditions in summer.

It is clear in spring that the MJO frequency is influenced by ENSO, with 169 days in enhanced rainfall phases 5 and 6 during El Niño, compared to 343 days during La Niña. In the suppressed rainfall phases 8, 1, and 2, there are 372 days during El Niño, compared to 207 during La Niña. One explanation behind this is the co-occurrence of El Niño and positive IOD events, where warm SST anomalies in the western tropical Indian Ocean support MJO development and easterly anomalies slow MJO propagation (e.g., Huang et al. 2022). The MJO propagation toward the eastern Indian Ocean is weaker during positive IOD events, compared to weak or negative IOD conditions, possibly due to the inhibition of low-level moisture convergence in the region (Wilson et al. 2013). As average MJO magnitudes in the enhanced and suppressed rainfall phases are similar between El Niño and La Niña in spring, the MJO amplitudes also cannot explain the difference in rainfall probabilities. This points to ENSO's strong influence on the MJO frequency in each phase in spring, but not its strength.

It is worth highlighting the moisture source regions that contribute to rainfall over Australia (Holgate et al. 2020b, 2022), and the role they play in contributing to the wet or dry conditions during MJO phases, albeit during El Niño or La Niña events. For example, in the 1997 El Niño year, despite weak MJO activity, southeast Australia experienced near-average rainfall, with three 10-mm days between August and September stemming from moist air drawn off the Coral Sea (Brown et al. 2009). This is an important summer moisture source for the Murray–Darling Basin and southern Australia (Holgate et al. 2020b). Over the Top End, moisture is sourced from the Indo-Pacific and Maritime Continent, as well as terrestrial sources. Over 1900–2018, the western warm pool has expanded by 80% with the MJO spending more than 5 days extra in the Indo-Pacific Maritime Continent (Roxy et al. 2019), meaning it can draw on these moisture sources, regardless of ENSO state.

Since 2010, northern Australia has experienced extreme wet and dry years, associated with central Pacific La Niña events in 2010–12 and central Pacific El Niño events in 2018–20 (Heidemann et al. 2022). With respect to the ENSO phases, the recent weakening in rainfall probabilities over the Top End and northwest regions associated with MJO phases 5 and 6 have predominantly occurred in the 6 years leading up to 2021 (as opposed to the period 2009–15), with the largest changes in La Niña and neutral summers (not shown). A recent study by Arushi et al. (2021) has shown a southward shift in the MJO variance over northern Australia over the period 1998–2015, which has coincided with the tropical Pacific entering a negative interdecadal Pacific oscillation phase and wetter wet seasons (November to April) over northern Australia (Sharmila and Hendon 2020). This suggests that the relationship between the enhanced MJO phases and northern Australian rainfall is nonstationary in time and likely is influenced by Pacific decadal variability, which could explain the apparent contrast between the changes identified in this study and those presented in Arushi et al. (2021).

The lack of a strong relationship between Australian rainfall and the SOI-defined ENSO in summer (e.g., McBride and Nicholls 1983; Risbey et al. 2009) might explain why little separates the enhanced rainfall probabilities over much of Australia between ENSO states. However, the significantly reduced rainfall probabilities during El Niño in MJO phases 8, 1, and 2 confirm the conclusions from Ghelani et al. (2017) that the MJO is more readily able to influence the large-scale atmosphere during an El Niño. Additionally, in the mature phase of an El Niño, positive rainfall anomalies in summer are not uncommon, particularly in the Northern Territory for eastern Pacific events and over southeast Australia for central Pacific events (Freund et al. 2021).

In our study, the combined influence of the IOD and MJO on enhancing or suppressing Australian rainfall is not evaluated. It is well accepted that co-occurring positive IOD and El Niño events are associated with reduced moisture over eastern and northern Australia in winter and spring (Risbey et al. 2009; Cai et al. 2011b; Holgate et al. 2022), with the opposite true for negative IOD and La Niña events. Hence, we can only speculate that spring rainfall variability in southern Queensland and the Top End is likely to have an IOD imprint alongside the MJO. Likewise, we have not considered partitioning the MJO using the phases of the quasi-biennial

oscillation (QBO). Other studies have shown a clear relationship between the QBO and MJO (Zhang and Zhang 2018; Martin et al. 2021), including the easterly QBO phase promoting stronger MJO convection from the Maritime Continent into the western Pacific in austral summer (Hendon and Abhik 2018). Understanding how this influences convective rainfall events presents an opportunity for future research.

It is anticipated that the updated MJO-related rainfall probability maps will help the BoM's customers make sense of the multiweek probabilistic rainfall forecasts, particularly if there is high probability of meaningful rainfall (Cowan et al. 2022). Yet while the updated maps will give users valuable information, there remains an issue with the simulated MJO teleconnection to parts of northern Australia in summer in the BoM's multiweek to seasonal forecast system, ACCESS-S1 (Marshall et al. 2021).[5] This is likely affecting the accuracy of the forecast MJO strength and its influence on the rainfall prediction in some instances (Lim et al. 2021b). As noted in Marshall et al. (2021), the skill in forecasting extreme weekly rainfall in summer across the central north, including the Gulf of Carpenteria region, is noticeably better when ACCESS-S1 predicts a weak MJO, compared to a strong MJO. An association between weaker MJO activity and better prediction skill in summer rainfall bursts is also evident in ACCESS-S1 across the northern tropics (Cowan et al. 2022). Low extended-range prediction skill in active MJO states, compared to inactive MJO states, is also an issue in other prediction systems over the U.S. West Coast (Pan et al. 2019), likely due to a simulated slowdown in its eastward movement over the Maritime Continent (Vitart and Molteni 2010; Wang et al. 2014). With this in mind, the updated MJO-related rainfall probability maps are better suited for placing historical events in context, than to be used as a statistical prediction tool.

5. Summary

In this study, we have produced new MJO average conditions maps to May 2022 using high-resolution (5 km) gridded observations to show the updated relationship between the eight MJO phases and Australian weekly rainfall. We have also investigated the combined influence of ENSO and the MJO on rainfall, extending the analysis of Ghelani et al. (2017). Our findings generally reflect those in Wheeler et al. (2009); in phases 4–6, when an active MJO pulse passes through the Maritime Continent to the western Pacific in austral summer and autumn, there is a higher chance of above median weekly rainfall over central and northern Australia. The results also suggest that the enhanced rainfall probabilities in phase 5 and 6 have weakened by up to 10% over the Top End in summer compared with earlier estimates from 1974 to 2009/10. At the same time, the MJO phases 2 and 3 in austral spring, which drive drier than usual conditions over southeast Australia, have weakened between 4% and 8% (i.e., less likely to be as dry). Therefore, in spring and summer, attempting to exploit the MJO to understand rainfall variability is now somewhat more difficult, although in other seasons, the relationship between MJO phases and rainfall probabilities has remained quite similar.

The combined ENSO–MJO results clearly support the earlier conclusions of Ghelani et al. (2017), whereby rainfall probabilities associated with the MJO across tropical Australia have larger swings during El Niño than La Niña—this predominantly occurs in the suppressed MJO phases 8, 1, and 2 in summer over the Top End, but also in winter and spring over central-southern Queensland. Interestingly, ENSO has little impact on the magnitude of the rainfall signal during the enhanced-rainfall MJO phases in summer. The interplay between ENSO events and the MJO is clearly seasonally and regionally dependent, and can be modulated by ENSO event type (Dasgupta et al. 2021).

Our findings, and the updated overlapping seasonal composite maps, will provide users with a more accurate depiction of the relationship between the MJO and Australian rainfall. Our study has also highlighted the importance of regularly updating average condition maps and maintaining a strong dialogue with customers using the BoM's weather and climate information to help interpreting rainfall forecasts for their region (Cobon et al. 2021). Through a better understanding of the observed MJO teleconnections and its impact on regional agriculture (e.g., Anderson et al. 2020), the BoM can continue to improve the multiweek prediction of the MJO and other intraseasonal phenomena.

Acknowledgments. This work is funded by Meat and Livestock Australia, the Queensland Government through the Drought and Climate Adaptation Program, and the University of Southern Queensland through the Northern Australia Climate Program (NACP). We extend our gratitude to the NACP Climate Mates for providing the motivation for us to undertake this research and are particularly grateful to Acacia Pepler and Roseanna McKay for reading and providing thought-provoking feedback on an early draft. We also extend our thanks to Stephanie Jacobs and Elise Chandler, who helped with improving the composite map code, and the three anonymous reviewers who provided valuable suggestions that greatly improved the manuscript. This research was undertaken with the assistance of resources from the National Computational Infrastructure Australia, a National Collaborative Research Infrastructure Strategy enabled capability supported by the Australian Government. The authors declare no conflicts of interest.

Data availability statement. The AGCD v1 rainfall data (1900–2018) are available from https://doi.org/10.4227/166/5a8647d1c23e0. The MJO index can be downloaded from http://www.bom.gov.au/climate/mjo/. Daily geopotential height and wind data are from NCEP–NCAR Reanalysis 1, available at https://psl.noaa.gov/data/gridded/data.ncep.reanalysis.surface.html. Interpolated OLR data are taken from NOAA/OAR/ESRL and can be downloaded from https://psl.noaa.gov/data/

[5] As of December 2021, a similar analysis has not been undertaken for ACCESS-S2, although skill in MJO prediction is nearly identical between ACCESS-S1 and -S2 (A. Marshall 2021, personal communication).

gridded/data.olrcdr.interp.html. The data in this study were analyzed in Python 3.10.0 and plotted using matplotlib. The code used to generate the maps is available from the corresponding author on reasonable request.

REFERENCES

Anderson, W., Á. G. Muñoz, L. Goddard, W. Baethgen, and X. Chourio, 2020: MJO teleconnections to crop growing seasons. *Climate Dyn.*, **54**, 2203–2219, https://doi.org/10.1007/s00382-019-05109-0.

An-Vo, D.-A., K. Reardon-Smith, S. Mushtaq, D. Cobon, S. Kodur, and R. Stone, 2019: Value of seasonal climate forecasts in reducing economic losses for grazing enterprises: Charters towers case study. *Rangeland J.*, **41**, 165–175, https://doi.org/10.1071/RJ18004.

Arushi, P. V., A. Chakraborty, and R. S. Nanjundiah, 2021: Recent weakening in MJO-related convective activity over the equatorial Indian Ocean and Maritime Continent. *Theor. Appl. Climatol.*, **143**, 267–278, https://doi.org/10.1007/s00704-020-03423-w.

Australian Bureau of Meteorology, 2019: Australian Gridded Climate Data (AGCD)/AWAP; v1.0.0 Snapshot (1900-01-01 to 2018-12-31). BoM, accessed 27 May 2021, https://doi.org/10.4227/166/5a8647d1c23e0.

Brown, J. N., P. C. McIntosh, M. J. Pook, and J. S. Risbey, 2009: An investigation of the links between ENSO flavors and rainfall processes in southeastern Australia. *Mon. Wea. Rev.*, **137**, 3786–3795, https://doi.org/10.1175/2009MWR3066.1.

——, A. Ash, N. MacLeod, and P. McIntosh, 2019: Diagnosing the weather and climate features that influence pasture growth in Northern Australia. *Climate Risk Manage.*, **24**, 1–12, https://doi.org/10.1016/j.crm.2019.01.003.

Cai, W., and T. Cowan, 2008: Evidence of impacts from rising temperature on inflows to the Murray-Darling Basin. *Geophys. Res. Lett.*, **35**, L07701, https://doi.org/10.1029/2008GL033390.

——, P. van Rensch, T. Cowan, and A. Sullivan, 2010: Asymmetry in ENSO teleconnection with regional rainfall, its multidecadal variability, and impact. *J. Climate*, **23**, 4944–4955, https://doi.org/10.1175/2010JCLI3501.1.

——, ——, and ——, 2011a: Influence of global-scale variability on the subtropical ridge over southeast Australia. *J. Climate*, **24**, 6035–6053, https://doi.org/10.1175/2011JCLI4149.1.

——, ——, ——, and H. H. Hendon, 2011b: Teleconnection pathways of ENSO and the IOD and the mechanisms for impacts on Australian rainfall. *J. Climate*, **24**, 3910–3923, https://doi.org/10.1175/2011JCLI4129.1.

Chung, C., and S. Power, 2017: The non-linear impact of El Niño, La Niña and the Southern Oscillation on seasonal and regional Australian precipitation. *J. South. Hemisphere Earth Syst. Sci.*, **67**, 25–45, https://doi.org/10.22499/3.6701.003.

Cobon, D. H., R. Darbyshire, J. Crean, S. Kodur, M. Simpson, and C. Jarvis, 2020: Valuing seasonal climate forecasts in the northern Australia beef industry. *Wea. Climate Soc.*, **12**, 3–14, https://doi.org/10.1175/WCAS-D-19-0018.1.

——, C. Jarvis, K. Reardon-Smith, L. Guillory, C. Pudmenzky, T. Nguyen-Huy, S. Mushtaq, and R. Stone, 2021: Northern Australia Climate Program: Supporting adaptation in rangeland grazing systems through more targeted climate forecasts, improved drought information and an innovative extension program. *Rangeland J.*, **43**, 87–100, https://doi.org/10.1071/RJ20074.

Cowan, T., R. Stone, M. C. Wheeler, and M. Griffiths, 2020: Improving the seasonal prediction of Northern Australian rainfall onset to help with grazing management decisions. *Climate Serv.*, **19**, 100182, https://doi.org/10.1016/j.cliser.2020.100182.

——, M. C. Wheeler, S. Sharmila, S. Narsey, and C. de Burgh-Day, 2022: Forecasting northern Australian summer rainfall bursts using a seasonal prediction system. *Wea. Forecasting*, **37**, 23–44, https://doi.org/10.1175/WAF-D-21-0046.1.

Darbyshire, R., and Coauthors, 2020: Insights into the value of seasonal climate forecasts to agriculture. *Aust. J. Agric. Resour. Econ.*, **64**, 1034–1058, https://doi.org/10.1111/1467-8489.12389.

Dasgupta, P., M. K. Roxy, R. Chattopadhyay, C. V. Naidu, and A. Metya, 2021: Interannual variability of the frequency of MJO phases and its association with two types of ENSO. *Sci. Rep.*, **11**, 11541, https://doi.org/10.1038/s41598-021-91060-2.

Dey, R., S. C. Lewis, J. M. Arblaster, and N. J. Abram, 2019: A review of past and projected changes in Australia's rainfall. *Wiley Interdiscip. Rev.: Climate Change*, **10**, e577, https://doi.org/10.1002/wcc.577.

Donald, A., H. Meinke, and B. Power, 2006: Near-global impact of the Madden–Julian Oscillation on rainfall. *Geophys. Res. Lett.*, **33**, L09704, https://doi.org/10.1029/2005GL025155.

Freund, M. B., B. J. Henley, D. J. Karoly, H. V. McGregor, N. J. Abram, and D. Dommenget, 2019: Higher frequency of Central Pacific El Niño events in recent decades relative to past centuries. *Nat. Geosci.*, **12**, 450–455, https://doi.org/10.1038/s41561-019-0353-3.

——, A. G. Marshall, M. C. Wheeler, and J. N. Brown, 2021: Central Pacific El Niño as a precursor to summer drought-breaking rainfall over southeastern Australia. *Geophys. Res. Lett.*, **48**, e2020GL091131, https://doi.org/10.1029/2020GL091131.

Ghelani, R. P. S., E. C. J. Oliver, N. J. Holbrook, M. C. Wheeler, and P. J. Klotzbach, 2017: Joint modulation of intraseasonal rainfall in tropical Australia by the Madden–Julian Oscillation and El Niño–Southern Oscillation. *Geophys. Res. Lett.*, **44**, 10 754–10 761, https://doi.org/10.1002/2017GL075452.

Griffiths, M., M. J. Reeder, D. J. Low, and R. A. Vincent, 1998: Observations of a cut-off low over Southern Australia. *Quart. J. Roy. Meteor. Soc.*, **124**, 1109–1132, https://doi.org/10.1002/qj.49712454805.

Gruber, A., and A. F. Krueger, 1984: The status of the NOAA outgoing longwave radiation data set. *Bull. Amer. Meteor. Soc.*, **65**, 958–962, https://doi.org/10.1175/1520-0477(1984)065<0958:TSOTNO>2.0.CO;2.

Heidemann, H., J. Ribbe, T. Cowan, B. J. Henley, C. Pudmenzky, R. Stone, and D. H. Cobon, 2022: The influence of interannual and decadal Indo-Pacific sea surface temperature variability on Australian monsoon rainfall. *J. Climate*, **35**, 425–444, https://doi.org/10.1175/JCLI-D-21-0264.1.

Hendon, H. H., and S. Abhik, 2018: Differences in vertical structure of the Madden–Julian Oscillation associated with the quasi-biennial oscillation. *Geophys. Res. Lett.*, **45**, 4419–4428, https://doi.org/10.1029/2018GL077207.

——, D. W. J. Thompson, and M. C. Wheeler, 2007: Australian rainfall and surface temperature variations associated with the Southern Hemisphere annular mode. *J. Climate*, **20**, 2452–2467, https://doi.org/10.1175/JCLI4134.1.

Holgate, C. M., A. I. J. M. Van Dijk, J. P. Evans, and A. J. Pitman, 2020a: Local and remote drivers of southeast Australian drought. *Geophys. Res. Lett.*, **47**, e2020GL090238, https://doi.org/10.1029/2020GL090238.

——, J. P. Evans, A. I. J. M. van Dijk, A. J. Pitman, and G. Di Virgilio, 2020b: Australian precipitation recycling and evaporative source regions. *J. Climate*, **33**, 8721–8735, https://doi.org/10.1175/JCLI-D-19-0926.1.

——, ——, A. S. Taschetto, A. Sen Gupta, and A. Santoso, 2022: The impact of interacting climate modes on east Australian precipitation moisture sources. *J. Climate*, **35**, 3147–3159, https://doi.org/10.1175/JCLI-D-21-0750.1.

Huang, Z., W. Zhang, C. Liu, and M. F. Stuecker, 2022: Extreme Indian Ocean dipole events associated with El Niño and Madden–Julian oscillation. *Climate Dyn.*, **59**, 1953–1968, https://doi.org/10.1007/s00382-022-06190-8.

Jaffrés, J. B. D., C. Cuff, C. Rasmussen, and A. S. Hesson, 2018: Teleconnection of atmospheric and oceanic climate anomalies with Australian weather patterns: A review of data availability. *Earth-Sci. Rev.*, **176**, 117–146, https://doi.org/10.1016/j.earscirev.2017.08.010.

Jones, D. A., W. Wang, and R. Fawcett, 2009: High-quality spatial climate data-sets for Australia. *Aust. Meteor. Oceanogr. J.*, **58**, 233–248, https://doi.org/10.22499/2.5804.003.

Kalnay, E., and Coauthors, 1996: The NCEP/NCAR 40-Year Reanalysis Project. *Bull. Amer. Meteor. Soc.*, **77**, 437–472, https://doi.org/10.1175/1520-0477(1996)077<0437:TNYRP>2.0.CO;2.

King, A. D., N. P. Klingaman, L. V. Alexander, M. G. Donat, N. C. Jourdain, and P. Maher, 2014: Extreme rainfall variability in Australia: Patterns, drivers, and predictability. *J. Climate*, **27**, 6035–6050, https://doi.org/10.1175/JCLI-D-13-00715.1.

Liebmann, B., and C. A. Smith, 1996: Description of a complete (interpolated) outgoing longwave radiation dataset. *Bull. Amer. Meteor. Soc.*, **77**, 1275–1277, https://doi.org/10.1175/1520-0477-77.6.1274.

Lim, E.-P., and Coauthors, 2021a: The 2019 Southern Hemisphere stratospheric polar vortex weakening and its impacts. *Bull. Amer. Meteor. Soc.*, **102**, E1150–E1171, https://doi.org/10.1175/BAMS-D-20-0112.1.

——, and Coauthors, 2021b: Why Australia was not wet during spring 2020 despite La Niña. *Sci. Rep.*, **11**, 18423, https://doi.org/10.1038/s41598-021-97690-w.

Lisonbee, J., and J. Ribbe, 2021: Seasonal climate influences on the timing of the Australian monsoon onset. *Wea. Climate Dyn.*, **2**, 489–506, https://doi.org/10.5194/wcd-2-489-2021.

Madden, R. A., and P. R. Julian, 1994: Observations of the 40–50-day tropical oscillation—A review. *Mon. Wea. Rev.*, **122**, 814–837, https://doi.org/10.1175/1520-0493(1994)122<0814:OOTDTO>2.0.CO;2.

Marshall, A. G., 2021: Lessons learned in outback Western Australia. *Bull. Aust. Meteor. Oceanogr. Soc.*, **34**, 22–24.

——, H. H. Hendon, and D. Hudson, 2021: Influence of the Madden–Julian Oscillation on multiweek prediction of Australian rainfall extremes using the ACCESS-S1 prediction system. *J. South. Hemisphere Earth Syst. Sci.*, **71**, 159–180, https://doi.org/10.1071/ES21001.

——, M. C. Wheeler, and T. Cowan, 2022: Madden–Julian oscillation impacts on Australian temperatures and extremes. *J. Climate*, **36**, 335–357, https://doi.org/10.1175/JCLI-D-22-0413.1.

Martin, Z., S.-W. Son, A. Butler, H. Hendon, H. Kim, A. Sobel, S. Yoden, and C. Zhang, 2021: The influence of the quasi-biennial oscillation on the Madden–Julian oscillation. *Nat. Rev. Earth Environ.*, **2**, 477–489, https://doi.org/10.1038/s43017-021-00173-9.

McBride, J. L., and N. Nicholls, 1983: Seasonal relationships between Australian rainfall and the Southern Oscillation. *Mon. Wea. Rev.*, **111**, 1998–2004, https://doi.org/10.1175/1520-0493(1983)111<1998:SRBARA>2.0.CO;2.

McKeon, G., G. Stone, D. Ahrens, J. Carter, D. Cobon, S. Irvine, and J. Syktus, 2021: Queensland's multi-year wet and dry periods: Implications for grazing enterprises and pasture resources. *Rangeland J.*, **43**, 121–142, https://doi.org/10.1071/RJ20089.

Moon, J.-Y., B. Wang, and K.-J. Ha, 2011: ENSO regulation of MJO teleconnection. *Climate Dyn.*, **37**, 1133–1149, https://doi.org/10.1007/s00382-010-0902-3.

Narsey, S., M. J. Reeder, D. Ackerley, and C. Jakob, 2017: A midlatitude influence on Australian monsoon bursts. *J. Climate*, **30**, 5377–5393, https://doi.org/10.1175/JCLI-D-16-0686.1.

Pan, B., K. Hsu, A. AghaKouchak, S. Sorooshian, and W. Higgins, 2019: Precipitation prediction skill for the West Coast United States: From short to extended range. *J. Climate*, **32**, 161–182, https://doi.org/10.1175/JCLI-D-18-0355.1.

Pook, M., S. Lisson, J. Risbey, C. C. Ummenhofer, P. McIntosh, and M. Rebbeck, 2009: The autumn break for cropping in southeast Australia: Trends, synoptic influences and impacts on yield. *Int. J. Climatol.*, **29**, 2012–2026, https://doi.org/10.1002/joc.1833.

Power, S., M. Haylock, R. Colman, and X. Wang, 2006: The predictability of interdecadal changes in ENSO activity and ENSO teleconnections. *J. Climate*, **19**, 4755–4771, https://doi.org/10.1175/JCLI3868.1.

Risbey, J. S., M. J. Pook, P. C. McIntosh, M. C. Wheeler, and H. H. Hendon, 2009: On the remote drivers of rainfall variability in Australia. *Mon. Wea. Rev.*, **137**, 3233–3253, https://doi.org/10.1175/2009MWR2861.1.

Roxy, M. K., P. Dasgupta, M. J. McPhaden, T. Suematsu, C. Zhang, and D. Kim, 2019: Twofold expansion of the Indo-Pacific warm pool warps the MJO life cycle. *Nature*, **575**, 647–651, https://doi.org/10.1038/s41586-019-1764-4.

Schwendike, J., G. J. Berry, K. Fodor, and M. J. Reeder, 2021: On the relationship between the Madden–Julian Oscillation and the Hadley and Walker circulations. *J. Geophys. Res. Atmos.*, **126**, e2019JD032117, https://doi.org/10.1029/2019JD032117.

Sharmila, S., and H. H. Hendon, 2020: Mechanisms of multiyear variations of Northern Australia wet-season rainfall. *Sci. Rep.*, **10**, 5086, https://doi.org/10.1038/s41598-020-61482-5.

Stone, G., R. D. Pozza, J. Carter, and G. McKeon, 2019: Long Paddock: Climate risk and grazing information for Australian rangelands and grazing communities. *Rangeland J.*, **41**, 225–232, https://doi.org/10.1071/RJ18036.

Stone, R. C., G. L. Hammer, and T. Marcussen, 1996: Prediction of global rainfall probabilities using phases of the Southern Oscillation Index. *Nature*, **384**, 252–255, https://doi.org/10.1038/384252a0.

Timbal, B., and W. Drosdowsky, 2013: The relationship between the decline of southeastern Australian rainfall and the strengthening of the subtropical ridge. *Int. J. Climatol.*, **33**, 1021–1034, https://doi.org/10.1002/joc.3492.

Troup, A. J., 1965: The Southern Oscillation. *Quart. J. Roy. Meteor. Soc.*, **91**, 490–506, https://doi.org/10.1002/qj.49709139009.

van Rensch, P., and W. Cai, 2014: Indo-Pacific–induced wave trains during austral autumn and their effect on Australian rainfall. *J. Climate*, **27**, 3208–3221, https://doi.org/10.1175/JCLI-D-13-00611.1.

Vitart, F., and F. Molteni, 2010: Simulation of the Madden–Julian Oscillation and its teleconnections in the ECMWF forecast system. *Quart. J. Roy. Meteor. Soc.*, **136**, 842–855, https://doi.org/10.1002/qj.623.

Wang, G., and H. H. Hendon, 2020: Impacts of the Madden–Julian Oscillation on wintertime Australian minimum temperatures and Southern Hemisphere circulation. *Climate Dyn.*, **55**, 3087–3099, https://doi.org/10.1007/s00382-020-05432-x.

Wang, W., M.-P. Hung, S. J. Weaver, A. Kumar, and X. Fu, 2014: MJO prediction in the NCEP Climate Forecast System version 2. *Climate Dyn.*, **42**, 2509–2520, https://doi.org/10.1007/s00382-013-1806-9.

Wheeler, M. C., and H. H. Hendon, 2004: An all-season real-time multivariate MJO index: Development of an index for monitoring and prediction. *Mon. Wea. Rev.*, **132**, 1917–1932, https://doi.org/10.1175/1520-0493(2004)132<1917:AARMMI>2.0.CO;2.

——, ——, S. Cleland, H. Meinke, and A. Donald, 2009: Impacts of the Madden–Julian oscillation on Australian rainfall and circulation. *J. Climate*, **22**, 1482–1498, https://doi.org/10.1175/2008JCLI2595.1.

Wilson, E. A., A. L. Gordon, and D. Kim, 2013: Observations of the Madden Julian Oscillation during Indian Ocean dipole events. *J. Geophys. Res. Atmos.*, **118**, 2588–2599, https://doi.org/10.1002/jgrd.50241.

Yuan, C., and T. Yamagata, 2015: Impacts of IOD, ENSO and ENSO Modoki on the Australian winter wheat yields in recent decades. *Sci. Rep.*, **5**, 17252, https://doi.org/10.1038/srep17252.

Zhang, C., 2005: Madden–Julian Oscillation. *Rev. Geophys.*, **43**, https://doi.org/10.1029/2004RG000158.

——, and B. Zhang, 2018: QBO–MJO connection. *J. Geophys. Res. Atmos.*, **123**, 2957–2967, https://doi.org/10.1002/2017JD028171.